POLITECNICO DI TORINO
Repository ISTITUZIONALE

An Imaging-Informed Mechanical Framework to Provide a Quantitative Description of Brain Tumour Growth and the Subsequent Deformation of White Matter Tracts

Original
An Imaging-Informed Mechanical Framework to Provide a Quantitative Description of Brain Tumour Growth and the Subsequent Deformation of White Matter Tracts / Ballatore, F., Lucci, G., Borio, A., Giverso, C. (SEMA SIMAI SPRINGER SERIES). - In: Mathematical Models and Computer Simulations for Biomedical Applications.[s.l] : Springer, 2023. - ISBN 978-3-031-35714-5. - pp. 131-169 [10.1007/978-3-031-35715-2_5]

Availability:
This version is available at: 11583/2981698 since: 2023-09-08T07:06:28Z

Publisher:
Springer

Published
DOI:10.1007/978-3-031-35715-2_5

Terms of use:

This article is made available under terms and conditions as specified in the corresponding bibliographic description in the repository

Publisher copyright
Springer postprint/Author's Accepted Manuscript (book chapters)

This is a post-peer-review, pre-copyedit version of a book chapter published in Mathematical Models and Computer Simulations for Biomedical Applications.. The final authenticated version is available online at: http://dx.doi.org/10.1007/978-3-031-35715-2_5

(Article begins on next page)

15 November 2026

An imaging-informed mechanical framework to provide a quantitative description of brain tumour growth and the subsequent deformation of white matter tracts

Francesca Ballatore, Giulio Lucci, Andrea Borio, Chiara Giverso

Abstract The mathematical description of brain tumours is a challenging problem, that may be fundamental to support medical observations and to build personalised therapeutic treatments for the patients. In this respect, we propose a multiphase model, based on Continuum Mechanics, where both the healthy and the diseased regions are treated as mixtures, comprising a solid and a fluid phase. Moreover, we use patient-specific imaging data to reconstruct the preferential directions for nutrient diffusion, fluid and cell motion inside the brain, since they all follow the orientation of white matter tracts. Then, given the mechanical deformation induced by the tumour onto the healthy tissue, we employ it to properly modify the preferential directions of white matter tracts. Our numerical simulations show that tumour-induced displacements and stresses may have a substantial impact on the tissue surrounding the cancer mass, even in regions distant from the tumour position. Furthermore, the model is able to highlight relevant changes in the preferential directions of nutrient diffusion and cell motion, caused by the spread of the cancer. Finally, the proposed framework may be a useful tool for the mechanical and computational modelling of other kinds of tumours growing in highly anisotropic environments and for estimating the effect of the expanding mass on the surrounding tissue.

Francesca Ballatore
Politecnico di Torino, Corso Duca degli Abruzzi 24, 10129 Torino, ITALY

Giulio Lucci
Politecnico di Torino, Corso Duca degli Abruzzi 24, 10129 Torino, ITALY

Andrea Borio
Politecnico di Torino, Corso Duca degli Abruzzi 24, 10129 Torino, ITALY

Chiara Giverso
Politecnico di Torino, Corso Duca degli Abruzzi 24, 10129 Torino, ITALY
e-mail: chiara.giverso@polito.it

1 Introduction

Despite the relevant advances in clinical practice supported by novel therapies and imaging techniques, the treatment of brain tumours remains not fully effective in many cases, due to cancer aggressiveness and to the intrinsically fragile nature of brain tissue. For this reason, in the last three decades, the mathematical modelling of brain tumour growth started to attract research attention. The purpose of these models is essentially twofold: first, they can help in understanding the progression of the tumour, providing further support to medical observations; then, *in silico* findings coming from simulations may be employed to build personalised therapeutic strategies, which are particularly important in the case of brain cancers to maximize the efficacy of treatments while minimizing side effects for the patients. In order to obtain a realistic outcome, the interplay between models and clinical data is crucial, as well as the accurate mathematical description of the brain environment, which is known to strongly affect tumour progression [22, 48, 78, 80].

To achieve these goals, models of brain tumour growth have become increasingly refined during the years: to give an overview, in Table 1 we summarise some of the main contributions that appear in the literature. For detailed and extensive reviews on brain cancer modelling, we refer the reader to [4, 37, 48, 66].

In particular, a first distinction between models can be made according to the mathematical framework they use, which is strictly related to the scale that is considered. More specifically, microscopic and mesoscopic models provide a description of phenomena taking place at the subcellular or cellular scale. These types of models mainly fulfill the objective of reproducing the early growth of brain tumours, accounting explicitly for interactions at the cellular level: most of them are Cellular Automata (CA), Agent-Based Models (ABM) or Ordinary Differential Equations (ODE) models. On the other hand, macroscopic models based on Partial Differential Equations (PDE) do not consider the intrinsically discrete nature of tumours, in exchange for a more flexible description performed through continuous variables. The first works [84–88, 92, 94] using reaction-diffusion equations for the migration and proliferation of gliomas paved the way for a number of subsequent studies, with an increasing level of detail. Multi-scale formulations bridging the gap between the microscopic and the macroscopic levels, grounded on Kinetic Models (KM) and their scaling [25, 26, 33–36, 52, 73, 83], also provided an interesting extension of purely diffusive, phenomenological descriptions. Another approach recently proposed to tackle the problem of brain tumour proliferation employs a Cahn-Hilliard-type (CH) equation to deal with the infiltrative nature of some brain tumours, showing a good agreement with real data [1–3, 24, 37].

As discussed above, a fundamental improvement to build reliable models for clinical applications is the inclusion of realistic imaging data, which may be used both for the estimation of parameters and for performing simulations on real geometries. In particular, the very first works [84–88, 92, 94] employed Computed Tomography (CT) and Magnetic Resonance Imaging (MRI) to extrapolate numerical values for the model parameters and to introduce a spatial distinction between white and grey matter. Then, the progress in Diffusion Tensor Imaging (DTI) allowed to account for

the intrinsic anisotropy of brain tissue and became of great interest in the modelling process [54].

Nevertheless, the majority of the models mentioned so far does not take into account the mechanical impact of the growing tumour mass on the healthy brain tissue. Instead, the deformation induced by the proliferating cancer onto the surrounding areas may be harmful for the patient, since it may lead to damage in brain functionalities. In this respect, recent experimental works [21, 70, 71, 78] pointed out the preeminent role of solid stresses due to brain tumour expansion, in addition to the effects of fluid pressure. Moreover, the distribution of such stresses appears to be different even in tumours that exhibit similar imaging volumes [71, 80]. Therefore, it is important to have models that are able to capture the mechanical effects of a tumour inside the skull, to precisely evaluate the brain area affected by the cancer and the consequent possible risks for the patient. Motivated by these facts, some recent models exploited the framework of Continuum Mechanics to provide a description of the so-called "mass effect" caused by the tumour. The first and simpler biomechanical models considered the brain as a linear elastic (LE) medium [16, 23, 50], while nonlinearly elastic (NLE) constitutive equations (e.g. Neo-Hookean or Mooney-Rivlin) have been employed in successive descriptions [9, 10, 30, 31, 62].

Another relevant feature that a quantitative mechanical model allows to introduce is the modification of DTI imaging data as a consequence of tumour growth [62]. Indeed, the growing mass displaces and dislodges the surrounding white matter fibres, causing a change in the preferential directions for water diffusion and cell movement. Since for patients affected by aggressive brain cancers it is often difficult to obtain multiple imaging scans at different times, the possibility of providing a computational modification of DTI data by means of mechanics may have valuable clinical implications.

Motivated by these observations, in this Chapter we propose a mechanical and computational framework which may be used to describe brain tumour growth, accounting both for a detailed mechanical representation and for the inclusion of patient-specific data. Specifically, we derive a multiphase model based on Continuum Mechanics which features the nonlinear elastic properties of brain tissue, being then able to quantify the deformation and the solid stress induced by the growing tumour. In our description, differently from previous models [62], the tumour is sharply separated from the host tissue, leading to variables of the model which are not necessarily continuous across the interface. It is therefore mandatory to specify proper interface conditions between the healthy and the cancer tissues, which also have distinct mechanical properties. Such a description is appropriate to represent solid brain tumours with a sharp separation between the cancer and the surrounding healthy area. Then, as already done in [62], we perform simulations on a realistic three-dimensional brain geometry reconstructed from MRI and DTI data and we employ the knowledge of the mechanical variables provided by our model to modify the DTI data in time, by changing the orientation of white matter fibres as a consequence of the deformation. We observe that the proposed framework may be used, properly modified, for the mechanical and computational modelling of other kinds of tumours growing in highly anisotropic environments.

In detail, the structure of the Chapter is as follows. In Section 2 we present the mathematical model and the governing equations, describing also the process of DTI data modification following the mechanical deformation. We remark that the introduction of discontinuous variables, due to the presence of two distinct domains, requires to pay attention to the derivation of the weak form of the problem, rewritten in the Lagrangian frame. Therefore, in Section 3 of the present work we provide details on the derivation of the weak formulation of the problem and on its discretisation in space and time. Then, always in Section 3, we provide a possible estimate for all the parameters involved in the model and we define the procedure used to create the patient-specific mesh. Section 4 is devoted to the presentation of some numerical outcomes, showing the validity of the proposed framework as a proof-of-concept for the mechanical description of brain tumours and DTI modification.

Type of Model	**References**	**Mechanics**	**Imaging**
CA	[11, 12, 17, 49, 55, 56, 91]	No	No
ODE	[14, 53]	No	No
ABM	[63–65]	No	No
ABM – PDE – RD	[42, 43]	No	No
PDE – RD	[76, 84–89, 92, 94]	No	Yes (CT+MRI)
PDE – RD	[47, 54]	No	Yes (MRI+DTI)
PDE – ARD	[95]	No	No
PDE – ARD	[82]	No	Yes (DTI)
PDE – ARD – KM	[73, 83]	No	Yes (DTI)
ODE – PDE – ARD – KM	[25, 26, 33–36, 52]	No	Yes (DTI)
PDE – ARD – CM	[16, 23, 32, 50]	Yes (LE)	Yes (MRI+DTI)
PDE – CM	[9, 10, 30, 31, 59, 62]	Yes (NLE)	Yes (MRI+DTI)
PDE – CM	[67]	Yes (FL)	No
PDE – CH	[1–3, 24, 37, 60]	Yes (FL)	Yes (MRI+DTI)
HYB	[40, 57, 58, 77]	No	No
HYB	[90, 96]	No	No

Table 1 Summary of previous contributions concerning brain tumour modelling. The models are classified according to three criteria: (i) the mathematical framework employed to describe the growth of the tumour mass (first column); (ii) the inclusion of tumour and tissue mechanics with quantification of deformations and stresses (third column); (iii) the use of patient-specific imaging data to perform simulations (fourth column). Abbreviations: CA = Cellular Automaton; ABM = Agent-Based Model; ODE = Ordinary Differential Equations model; PDE-RD = Reaction-Diffusion equations; PDE-ARD = Advection-Reaction-Diffusion equations; PDE-KM = Kinetic model; PDE-CH = Cahn-Hilliard model; PDE-CM = Continuum-Mechanics-based model; HYB = Hybrid model; FL = Fluid; LE = Linear elasticity; NLE = Nonlinear elasticity.

2 A multiphase model for brain tumour growth

In this Section, we present a multiphase model for tumour growth and expansion, based on the theory of mixtures [6, 19, 75] and consisting of a set of mass and momentum balance equations. Even though the general framework of the proposed model could be used, in principle, to describe the development of any kind of solid tumour, we specialise it to account for brain tumour evolution in a patient-specific setting. The aim of the mathematical model presented hereafter is to evaluate the progression of this disease, in order to predict the evolution of tumour shape and to quantify the extent and the position of damaged areas. We assume that the region occupied by the tumour, denoted by $\Omega_t(t)$, is completely separated from the healthy host tissue, denoted by $\Omega_h(t)$, so that the boundary between the tumour and the surrounding environment can be described by a moving interface. Both these regions are treated as saturated domains consisting of two distinct phases, representing the cell population (labelled with subscript "s") and the interstitial fluid (labelled with subscript "ℓ"), which fill all the available space. Therefore, introducing the volumetric fraction of the cell population, ϕ_s, and the volumetric fraction of the liquid, ϕ_ℓ, the saturation constraint

$$\phi_s + \phi_\ell = 1 \tag{1}$$

holds at any time instant and at any point in the brain domain $\Omega(t) = \Omega_h(t) \cup \Omega_t(t)$. We remark that, in this description, the cellular phase represents healthy cells in $\Omega_h(t)$ and diseased cells in $\Omega_t(t)$, whereas the fluid phase resumes interstitial brain fluid, blood, and nutrients in both regions. Furthermore, we assume that the materials composing the phases are incompressible, which means that both phases of the mixture have constant true densities $\hat{\rho}_\alpha$, with $\alpha \in \{s, \ell\}$. Then, once the true density $\hat{\rho}_\alpha$ is prescribed, the partial phase density $\rho_\alpha := \hat{\rho}_\alpha \phi_\alpha$ of the material composing the α-phase is totally defined by knowing ϕ_α. Finally, since cells are mainly composed of water, we assume that the true densities of both phases are equal, i.e., $\hat{\rho}_s = \hat{\rho}_\ell$.
Throughout this Chapter, we will denote by Ω^*, Ω_t^* and Ω_h^* the reference configurations of the whole brain, the tumour and the host tissue, respectively, so that $\Omega^* = \Omega_h^* \cup \Omega_t^*$ holds. It is important to underline that the tumour region Ω_t^* in the reference configuration does not evolve in time. For what concerns the differential operators, Grad and Div will be used in the following to denote the material gradient and material divergence with derivatives taken with respect to the material point in the reference configuration. Instead, the notations ∇ and $\nabla\cdot$ will denote the gradient and the divergence with respect to the spatial variable in the current configuration $\Omega(t)$. The deformation of the body from the reference configuration to the deformed one can be described using the map $\chi(\mathbf{X}, t)$, which assigns to each material point $\mathbf{X} \in \Omega^*$ its position $\mathbf{x}$ in $\Omega(t)$. Introducing the displacement field of the solid phase, defined by $\mathbf{u}_s(\mathbf{X}, t) = \chi(\mathbf{X}, t) - \mathbf{X}$, we can define the *deformation gradient tensor* of the solid phase as $\mathbb{F}_s = \mathbb{I} + \mathrm{Grad}\, \mathbf{u}_s$, where $\mathbb{I}$ is the second order identity tensor. Moreover, the concept of evolving natural configurations is employed in the following to properly describe the mechanics of the growing body. Resorting to the modelling background proposed in [7, 8] for growing tumours, this approach consists

in splitting the evolution in pure elastic deformations and deformations subsequent to anelastic distortions, such as growth and remodelling. In particular, if we assume to cut a generic particle out of the body and to relieve its state of stress while keeping the mass constant, we find the *natural state* of such particle at time t. The *natural configuration* of the body at time t is then the collection of all the particles in their natural states at time t and it is indicated by $\Omega^{\mathrm{n}}(t)$. In this way it is possible to measure the deformation from the natural configuration $\Omega^{\mathrm{n}}(t)$ to $\Omega(t)$ through the tensor $\mathbb{F}_{\mathrm{e}}$, which is connected to the stress response of the material, while the path from the reference configuration Ω^* to the natural configuration is described by the tensor $\mathbb{F}_{\mathrm{g}}$, which is directly related to growth and it is therefore named *growth tensor*. This decomposition is graphically shown in Fig. 1. To sum up, the deformation

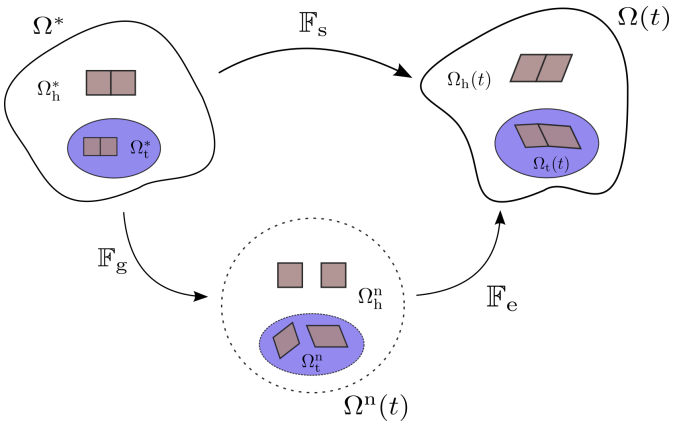


Fig. 1 Multiplicative decomposition of the deformation gradient.

gradient $\mathbb{F}_{\mathrm{s}}$ indicates how the body is deforming locally in going from the reference configuration Ω^* to $\Omega(t)$, while, in an analogous way, $\mathbb{F}_{\mathrm{e}}$ tells how the body is deforming locally in going from the natural configuration $\Omega^{\mathrm{n}}(t)$ to $\Omega(t)$, and $\mathbb{F}_{\mathrm{g}}$ tells how the body is growing locally. The following multiplicative decomposition of the deformation gradient is therefore valid:

$$\mathbb{F}_{\mathrm{s}} = \mathbb{F}_{\mathrm{e}}\mathbb{F}_{\mathrm{g}}\,. \tag{2}$$

Furthermore, since the deformation gradient $\mathbb{F}_{\mathrm{s}}$ is invertible, it follows that $\mathbb{F}_{\mathrm{e}}$ and $\mathbb{F}_{\mathrm{g}}$ are invertible too. Indeed, the determinant of the deformation gradient can be expressed as

$$J_{\mathrm{s}} = J_{\mathrm{e}}J_{\mathrm{g}}\,,$$

where $J_{\mathrm{e}} = \det\mathbb{F}_{\mathrm{e}}$ and $J_{\mathrm{g}} = \det\mathbb{F}_{\mathrm{g}}$. In particular, since we are dealing with growth processes, we have $J_{\mathrm{g}} \geq 1$.

2.1 Eulerian formulation

2.1.1 Balance equations

Mass and momentum balance laws in the tumour region $\Omega_t(t)$

To derive the balance equations of our model, we firstly focus on the region occupied by the tumour. We assume that, in this region, cells proliferate since the tumour is growing. Hence, the mass and momentum balances for each phase $\alpha \in \{s, \ell\}$ read

$$\frac{\partial \phi_\alpha}{\partial t} + \nabla \cdot (\phi_\alpha \mathbf{v}_\alpha) = \Gamma_\alpha \,, \tag{3}$$

$$\hat{\rho}_\alpha \phi_\alpha \left(\frac{\partial \mathbf{v}_\alpha}{\partial t} + \mathbf{v}_\alpha \cdot \nabla \mathbf{v}_\alpha \right) = \nabla \cdot \widetilde{\mathbb{T}}_\alpha + \hat{\rho}_\alpha \phi_\alpha \mathbf{b}_\alpha + \widetilde{\mathbf{m}}_\alpha \,, \tag{4}$$

where $\mathbf{v}_\alpha$ is the velocity of the α-phase, $\widetilde{\mathbb{T}}_\alpha$ is the partial Cauchy stress tensor of that phase, Γ_α is the mass growth rate and $\widetilde{\mathbf{m}}_\alpha$ represents the rate at which the α-phase exchanges momentum with the other phase. Then, the mixture is assumed to be closed with respect to mass, i.e., $\Gamma_\ell = -\Gamma_s$, so that mass exchanges occur only among the constituents taken into account. Moreover, external body forces (such as the gravitational force) included in $\mathbf{b}$ as well as inertial effects are negligible, since the motion of cells and interstitial fluid is very slow, when dealing with biological growth phenomena. Thus, Equation (4) becomes

$$\nabla \cdot \widetilde{\mathbb{T}}_\alpha + \widetilde{\mathbf{m}}_\alpha = \mathbf{0} \,. \tag{5}$$

The term $\widetilde{\mathbf{m}}_\alpha$, with $\alpha \in \{s, \ell\}$, can be decomposed, using thermodynamics arguments [44], into a dissipative and a non-dissipative part as $\widetilde{\mathbf{m}}_\alpha = \overline{\mathbf{m}}_{\alpha\beta} + p\nabla\phi_\alpha$, where p is the pressure of the interstitial fluid and the term $\overline{\mathbf{m}}_{\alpha\beta}$ represents the dissipative force acting on the α phase due to the other phase, denoted by subscript β. By invoking the action-reaction principle and the saturation condition (1), it holds that

$$\overline{\mathbf{m}}_{s\ell} = -\overline{\mathbf{m}}_{\ell s} \,. \tag{6}$$

We remark that, in defining the momentum exchange between phases, we neglected the exchange rates associated with the mass sources and sinks Γ_α, $\alpha \in \{s, \ell\}$. Such an assumption is reasonable in the context of avascular tumour growth, in which the velocities of both the solid and the fluid phase are small [44].

Following standard arguments in mixture theory, the Cauchy stress associated with the α-phase of the mixture can be written as the sum of a purely hydrostatic contribution, which indicates the amount of pressure sustained by the α-phase, and an effective stress

$$\widetilde{\mathbb{T}}_\alpha = -\phi_\alpha p \mathbb{I} + \mathbb{T}_\alpha \,.$$

Moreover, we require that the effective stress of the fluid phase $\mathbb{T}_\ell$ is negligible with respect to the pressure gradient and to the interaction forces between fluid and solid

phase. As a consequence, Eq. (5), specialised for the two phases, becomes

$$-\phi_{\mathrm{s}}\nabla p + \nabla \cdot \mathbb{T}_{\mathrm{s}} + \overline{\mathbf{m}}_{\mathrm{s}\ell} = \mathbf{0}\,, \tag{7}$$

$$-\phi_{\ell}\nabla p + \overline{\mathbf{m}}_{\ell\mathrm{s}} = \mathbf{0}\,. \tag{8}$$

The momentum balance for the mixture can then be obtained by summing (7) and (8), recalling the saturation condition (1) and the action-reaction principle (6):

$$-\nabla p + \nabla \cdot \mathbb{T}_{\mathrm{s}} = \mathbf{0}\,. \tag{9}$$

Furthermore, calling μ the dynamic viscosity of the fluid component, $\mathbb{K}(\phi_\ell)$ the permeability tensor and taking $\overline{\mathbf{m}}_{\ell\mathrm{s}} = -\mu\phi_\ell^2\mathbb{K}(\phi_\ell)^{-1}(\mathbf{v}_\ell - \mathbf{v}_{\mathrm{s}})$ [44], it is possible to derive from (8) the well-known Darcy's law as a momentum balance for the fluid phase

$$\mathbf{v}_\ell = \mathbf{v}_{\mathrm{s}} - \frac{\mathbb{K}(\phi_\ell)}{\mu\phi_\ell}\nabla p\,. \tag{10}$$

To account for the anisotropy in the fluid motion due to the presence of white and grey matter fibres in the brain tissue, we take the permeability tensor as

$$\mathbb{K}(\phi_\ell) := K(\phi_\ell)\,\mathbb{A}\,, \tag{11}$$

where $\mathbb{A}$ denotes the Eulerian preferential directions tensor [24], whose construction will be discussed in Section 2.1.4.

Mass and momentum balance laws in the healthy region $\Omega_{\mathrm{h}}(t)$

In the domain occupied by the healthy tissue we assume that the proliferation of cells is compensated by natural cell death, so that the net rate of growth is equal to zero (i.e. $\Gamma_{\mathrm{s}} = 0$). The closed mixture assumption implies that also the source term Γ_ℓ must be null. Hence, the mass balances in the healthy region can be written as

$$\frac{\partial\phi_\alpha}{\partial t} + \nabla\cdot(\phi_\alpha\mathbf{v}_\alpha) = 0\,, \quad \text{with}\,\alpha \in \{\mathrm{s},\ell\}\,.$$

As regards the momentum balance equations, they are the same as in the region occupied by the tumour, namely Equations (9) and (10). The differences in the mechanical properties between the healthy and the diseased tissues, affecting the stress tensor $\mathbb{T}_{\mathrm{s}}$, will be provided through the constitutive equations.

2.1.2 Stress tensor and constitutive equations

In order to close the system of mass and momentum balance equations and to understand how brain tumour growth influences mechanically the surrounding tissues, we have to determine an appropriate evolution law for the effective part of the Cauchy

stress tensor $\mathbb{T}_s$, associated with the cellular population, both in the diseased and in the healthy region. In analogy with [7], we assume that the mechanical response is hyperelastic from the natural configuration, that is, both the healthy brain tissue and the tumour are modelled as nonlinear elastic materials.

Effective stress tensor in $\Omega_t(t)$

In order to fully describe the elastic response, the generalized Ogden model [72] is often considered appropriate to represent the mechanical behaviour of soft brain tissue [69]. In particular, we take into account the Mooney-Rivlin model, which represents a particular case of the generalized Ogden energy [13, 27, 69]. Let $\overline{\mathbb{C}}_e := J_e^{-\frac{2}{3}}\mathbb{C}_e$ be the isochoric part of the elastic right Cauchy-Green deformation tensor $\mathbb{C}_e := \mathbb{F}_e^T\mathbb{F}_e$. The strain energy density per unit volume of the natural configuration $\widehat{\mathcal{W}}_{sn}$ can be written as a function of the first two invariants of $\overline{\mathbb{C}}_e$ and J_e:

$$\begin{aligned}\widehat{\mathcal{W}}_{sn}\left(\overline{\mathbb{C}}_e, J_e\right) = \frac{1}{2}\mu_{1t}\left(\mathrm{I}_{\overline{\mathbb{C}}_e} - 3\right) + \frac{1}{2}\mu_{2t}\left(\mathrm{II}_{\overline{\mathbb{C}}_e} - 3\right) + \\ + \kappa_t\left(1-\phi_{sn}\right)^2\left(\frac{J_e-1}{1-\phi_{sn}} - \ln\frac{J_e-\phi_{sn}}{1-\phi_{sn}}\right),\end{aligned} \tag{12}$$

where

$$\mathrm{I}_{\overline{\mathbb{C}}_e} := \mathrm{tr}\left(\overline{\mathbb{C}}_e\right), \qquad \mathrm{II}_{\overline{\mathbb{C}}_e} := \frac{1}{2}\left[\left(\mathrm{tr}\,\overline{\mathbb{C}}_e\right)^2 - \mathrm{tr}\left(\overline{\mathbb{C}}_e^2\right)\right].$$

The last term on the right-hand side of Eq. (12), which is different from the one employed in previous works (e.g. [62]), describes volumetric changes in the solid skeleton, occurring below the compaction point, i.e., when all pores in the structure are closed and further volume deformations are impeded due to the incompressibility of the solid phase (see [29] for further details). Furthermore, ϕ_{sn} represents the volumetric fraction of the cell phase in the natural state and it has a constant value. Finally, μ_{1t} and μ_{2t} are the material parameters of the tumour tissue whereas κ_t is the elastic parameter associated with the response of the tumour to volumetric deformations. Given $\widehat{\mathcal{W}}_{sn}$, we can express the Cauchy stress tensor of the cellular phase as

$$\mathbb{T}_s = 2J_e^{-1}\mathbb{F}_e\frac{\partial\widehat{\mathcal{W}}_{sn}}{\partial\mathbb{C}_e}\mathbb{F}_e^T \quad \text{in } \Omega_t(t). \tag{13}$$

By working out the derivative in (13) we have

$$\begin{aligned}\frac{\partial\widehat{\mathcal{W}}_{sn}\left(\overline{\mathbb{C}}_e, J_e\right)}{\partial\mathbb{C}_e} &= \frac{\partial\overline{\mathbb{C}}_e}{\partial\mathbb{C}_e} : \frac{\partial\widehat{\mathcal{W}}_{sn}}{\partial\overline{\mathbb{C}}_e} + \frac{\partial J_e}{\partial\mathbb{C}_e}\frac{\partial\widehat{\mathcal{W}}_{sn}}{\partial J_e} \\ &= J_e^{-2/3}\left(\underline{\underline{\mathbb{I}}} - \frac{1}{3}\overline{\mathbb{C}}_e^{-1}\otimes\overline{\mathbb{C}}_e\right) : \frac{\partial\widehat{\mathcal{W}}_{sn}}{\partial\overline{\mathbb{C}}_e} + \frac{1}{2}J_e\mathbb{C}_e^{-1}\frac{\partial\widehat{\mathcal{W}}_{sn}}{\partial J_e},\end{aligned}$$

where $\underline{\underline{\mathbb{I}}}$ is the fourth-order identity tensor. For the particular choice of material constitutive relation (12), we have

$$\frac{\partial \widehat{\mathcal{W}}_{\text{sn}}}{\partial \overline{\mathbb{C}}_{\text{e}}} = \frac{\partial \widehat{\mathcal{W}}_{\text{sn}}}{\partial \mathrm{I}_{\overline{\mathbb{C}}_{\text{e}}}} \mathbb{I} + \frac{\partial \widehat{\mathcal{W}}_{\text{sn}}}{\partial \mathrm{II}_{\overline{\mathbb{C}}_{\text{e}}}} \left(\mathrm{I}_{\overline{\mathbb{C}}_{\text{e}}} \mathbb{I} - \overline{\mathbb{C}}_{\text{e}} \right) = \frac{1}{2} \mu_{1\text{t}} \mathbb{I} + \frac{1}{2} \mu_{2\text{t}} \left(\mathrm{I}_{\overline{\mathbb{C}}_{\text{e}}} \mathbb{I} - \overline{\mathbb{C}}_{\text{e}} \right),$$
$$\frac{\partial \widehat{\mathcal{W}}_{\text{sn}}}{\partial J_{\text{e}}} = \kappa_{\text{t}} \left(1 - \phi_{\text{sn}}\right) \left(1 - \frac{1 - \phi_{\text{sn}}}{J_{\text{e}} - \phi_{\text{sn}}} \right).$$

Thus, the constitutive expression of the Cauchy stress tensor $\mathbb{T}_{\text{s}}$ becomes

$$\begin{aligned} \mathbb{T}_{\text{s}} = 2 J_{\text{e}}^{-1} \mathbb{F}_{\text{e}} \left[J_{\text{e}}^{-2/3} \left(\underline{\underline{\mathbb{I}}} - \frac{1}{3} \overline{\mathbb{C}}_{\text{e}}^{-1} \otimes \overline{\mathbb{C}}_{\text{e}} \right) : \left(\gamma_1 \mathbb{I} + \gamma_2 \overline{\mathbb{C}}_{\text{e}} \right) \right] \mathbb{F}_{\text{e}}^{\text{T}} + \\ + \kappa_{\text{t}} \left(1 - \phi_{\text{sn}}\right) \left(1 - \frac{1 - \phi_{\text{sn}}}{J_{\text{e}} - \phi_{\text{sn}}} \right) \mathbb{I}, \end{aligned} \tag{14}$$

where we have defined the quantities $\gamma_1 := \frac{1}{2} \mu_{1\text{t}} + \frac{1}{2} \mathrm{I}_{\overline{\mathbb{C}}_{\text{e}}} \mu_{2\text{t}}$ and $\gamma_2 := -\frac{1}{2} \mu_{2\text{t}}$. The constitutive expression of the Cauchy stress tensor should be accompanied by equations determining $\mathbb{F}_{\text{s}}$ and $\mathbb{F}_{\text{g}}$. The tensor $\mathbb{F}_{\text{s}}$ is entirely determined by the motion of the cell phase and for this reason it is not an additional unknown for the model. In fact, it satisfies

$$\dot{\mathbb{F}}_{\text{s}} \mathbb{F}_{\text{s}}^{-1} = \nabla \mathbf{v}_{\text{s}}.$$

So it remains to determine $\mathbb{F}_{\text{g}}$ by solving appropriate evolution equations. The evolution of $\mathbb{F}_{\text{g}}$ can be derived from Eq. (3) with $\alpha = \text{s}$. It is possible to show that the following relation has to hold [44, 68]:

$$\operatorname{tr}\left(\mathbb{L}_{\text{g}} \right) = \frac{\Gamma_{\text{s}}}{\phi_{\text{s}}}, \tag{15}$$

where $\mathbb{L}_{\text{g}} := \dot{\mathbb{F}}_{\text{g}} \mathbb{F}_{\text{g}}^{-1}$ is the strain rate tensor (or velocity gradient) associated with $\mathbb{F}_{\text{g}}$. In this work, we consider an isotropic growth tensor of the form

$$\mathbb{F}_{\text{g}} = g \mathbb{I}, \tag{16}$$

with g being a scalar field to be determined. Therefore, Eq. (16) leads to $\operatorname{tr}\left(\mathbb{L}_{\text{g}} \right) = 3 \dot{g} g^{-1}$, which consequently yields [8]

$$\frac{\dot{g}}{g} = \frac{1}{3} \frac{\Gamma_{\text{s}}}{\phi_{\text{s}}}, \quad \text{in } \Omega_{\text{t}}(t). \tag{17}$$

Equation (17) is an ordinary differential equation that, equipped with an initial condition, determines g uniquely. Hence, it completely determines the evolution of the growth tensor $\mathbb{F}_{\text{g}}$. Of course, this is true provided that Γ_{s} is given constitutively. In particular, we assume the following constitutive equation for the latter:

$$\Gamma_{\text{s}} = \nu \phi_{\text{s}} \left(\phi_{\max} - \phi_{\text{s}} \right) \left(c_n - c_0 \right)_+, \tag{18}$$

where $(\cdot)_+$ denotes the positive part and ν is a positive coefficient. In particular, we have that the proliferation rate depends linearly on the available concentration of nutrients c_n, provided that it is greater than the hypoxia threshold c_0, below which tumour cells stop duplicating. On the other hand, as long as $c_n > c_0$, the cell phase is allowed to grow and the proliferation rate is proportional to the difference between the actual nutrients concentration and the hypoxia threshold. Moreover, the growth rate depends on the fraction of cells that is already present, since cell population grows by duplication of existing cells, and on the availability of space that can be filled by the cellular phase. Therefore proliferation reduces as ϕ_s approaches the maximum admissible cell volume fraction $\phi_{max} \in (0, 1]$, for which contact inhibition of growth occurs. For more details about the definition of Γ_s, see [24,62] and references therein.

Effective stress tensor in $\Omega_h(t)$

In the host healthy tissue, as stated before, the net source term Γ_s is null, since the death of healthy cells is compensated by proliferation. This implies that, in principle, the multiplicative decomposition (2) is not needed in $\Omega_h(t)$. However, for simplicity, in order to have all quantities defined on both the tumour and the healthy tissue, it is possible to apply a fictitious multiplicative decomposition of the deformation gradient $\mathbb{F}_s$, by taking $\mathbb{F}_g = \mathbb{I}$ in $\Omega_h(t)$. Then, even though the constitutive mechanical model for the healthy tissue might be taken as totally different from the one describing the tumour, we assume that the solid phase is described by a Mooney-Rivlin strain energy density function $\widehat{\mathcal{W}}_{sn}$ as in (12) also in the healthy domain. Nevertheless, even assuming the same functional form, the material parameters could be different, i.e., we could use μ_{1h}, μ_{2h} and κ_h different from μ_{1t}, μ_{2t} and κ_t, respectively.

2.1.3 Nutrients

The rate of tumour growth Γ_s is influenced by many different factors, but of course the amount of nutrients plays a fundamental role, because it strongly affects the cells capability to duplicate. Consequently, it is necessary to introduce in the model an equation describing nutrients evolution in the domain. We assume that they are transported by the fluid phase and they can diffuse into it. On the other side, they are taken by the growing tumour and uniformly supplied by blood vessels. We introduce the hypothesis that the nutrients absorbed by the healthy tissue are immediately replaced by the vasculature, whereas the nutrients uptake by the tumour tissue is not negligible. Following these assumptions, we can write the mass balance equation governing the concentration of available nutrients c_n in $\Omega(t)$, normalising it with respect to the physiological concentration taken at the border of the brain:

$$\frac{\partial}{\partial t}(\phi_\ell c_n) + \nabla \cdot (\phi_\ell c_n \mathbf{v}_\ell) = \nabla \cdot (\phi_\ell \mathbb{D} \nabla c_n) + \Gamma_\ell c_n + G_n\,, \tag{19}$$

where $\mathbb{D}$ is the Eulerian diffusion tensor (discussed later in Section 2.1.4), the term $\Gamma_\ell c_n$ is related to the variation of the nutrients amount due to absorption/production of the liquid in which the chemical is dissolved, and G_n is the chemical source term occurring without net variation of the liquid amount. In particular, we will consider the form

$$G_n = \begin{cases} -\zeta \phi_\mathrm{s} \phi_\ell c_n + S_n \left(1 - c_n\right) \phi_\ell & \text{in } \Omega_\mathrm{t}(t) \\ 0 & \text{in } \Omega_\mathrm{h}(t) \end{cases} . \tag{20}$$

The expression of G_n in the tumour domain describes the fact that nutrients are consumed by the tumour with a constant rate ζ. Furthermore, nutrients are supplied at a rate S_n as far as their concentration is below the physiological value, whereas above the physiological value they are absorbed. The consumption and the delivery of nutrients is also weighted with a factor ϕ_ℓ to describe the fact that if there is a higher availability of fluid phase, then a greater uptake or supply of nutrients can be provided. On the other hand, in the healthy region we assume that production and absorption of nutrients are reciprocally balanced. Using standard calculus techniques and recalling the mass balance equation of the fluid phase, with $\Gamma_\ell = 0$ in $\Omega_\mathrm{h}(t)$, we can rewrite Eq. (19) in the tumour and in the healthy domain as

$$\frac{\partial c_n}{\partial t} + \mathbf{v}_\ell \cdot \nabla c_n = \frac{1}{\phi_\ell} \nabla \cdot (\phi_\ell \mathbb{D} \nabla c_n) + \left[-\zeta \phi_\mathrm{s} c_n + S_n \left(1 - c_n\right)\right] \qquad \text{in } \Omega_\mathrm{t}(t)\,, \tag{21a}$$

$$\frac{\partial c_n}{\partial t} + \mathbf{v}_\ell \cdot \nabla c_n = \frac{1}{\phi_\ell} \nabla \cdot (\phi_\ell \mathbb{D} \nabla c_n) \qquad \text{in } \Omega_\mathrm{h}(t)\,. \tag{21b}$$

2.1.4 Diffusion tensor $\mathbb{D}$ and preferential directions tensor $\mathbb{A}$

We still need to provide a definition for the diffusion tensor $\mathbb{D}$, appearing in Eq. (19), and for the tensor of preferential directions $\mathbb{A}$, which affects the permeability tensor $\mathbb{K}$ in Eq. (11). Since the displacement induced by the tumour modifies the direction of brain fibres in the surrounding environment and therefore alters the directions along which diffusion and fluid motion happen, we take advantage of the mechanical description included in our model to progressively modify these tensors as time evolves. The diffusion tensor at the initial time instant $\mathbb{D}_0$ can be constructed from DTI imaging data, through a computational processing summarised in Section 3.4. Indeed, DTI scan quantifies the diffusion of water inside the brain and for this reason it seems appropriate to employ such data to describe nutrients diffusion and to determine the orientation of nerve tracts and other structures inside the brain. Thus, we can write

$$\mathbb{D}_0 = \lambda_1^0 \mathbf{e}_1^0 \otimes \mathbf{e}_1^0 + \lambda_2^0 \mathbf{e}_2^0 \otimes \mathbf{e}_2^0 + \lambda_3^0 \mathbf{e}_3^0 \otimes \mathbf{e}_3^0\,,$$

where we call $\lambda_1^0 > \lambda_2^0 > \lambda_3^0$ the decreasing order eigenvalues and $\mathbf{e}_1^0, \mathbf{e}_2^0, \mathbf{e}_3^0$ the corresponding orthogonal eigenvectors of the initial tensor $\mathbb{D}_0$, taken from DTI images. The construction of $\mathbb{A}_0$, i.e. the initial value of tensor $\mathbb{A}$, is also performed using these data: the aim is to evaluate the preferential directions identified by the presence of white matter tracts. In particular, it is assumed that $\mathbb{A}_0$ has the same

eigenvectors as the diffusion tensor, while the eigenvalues are properly rescaled to enhance anisotropy along the preferential directions, as described in [1, 2, 54]. The tensor $\mathbb{A}_0$ is then defined as

$$\mathbb{A}_0 = \frac{1}{\mathrm{A}_{av}}\widehat{\mathbb{A}}_0, \quad \widehat{\mathbb{A}}_0 = a_1^0(r)\lambda_1^0\mathbf{e}_1^0\otimes\mathbf{e}_1^0 + a_2^0(r)\lambda_2^0\mathbf{e}_2^0\otimes\mathbf{e}_2^0 + \lambda_3^0\mathbf{e}_3^0\otimes\mathbf{e}_3^0, \quad \mathrm{A}_{av} = \frac{1}{3}\,\mathrm{tr}(\widehat{\mathbb{A}}_0),$$

where r is the tuning parameter of anisotropy and $a_i^0(r)$ are functions of r given by

$$a_1^0(r) = rc_l^0 + rc_p^0 + c_s^0\,, \quad a_2^0(r) = c_l^0 + rc_p^0 + c_s^0\,, \tag{22}$$

being c_l^0, c_p^0, c_s^0 the linear, planar and spherical anisotropy coefficients, respectively, defined as [54]:

$$c_l^0 = \frac{\lambda_1^0 - \lambda_2^0}{\lambda_1^0+\lambda_2^0+\lambda_3^0}\,, \quad c_p^0 = \frac{2(\lambda_2^0 - \lambda_3^0)}{\lambda_1^0+\lambda_2^0+\lambda_3^0}\,, \quad c_s^0 = \frac{3\lambda_3^0}{\lambda_1^0+\lambda_2^0+\lambda_3^0}\,.$$

Hence, the case $r = 1$ corresponds to a situation where the anisotropy is not increased, and therefore the tensor $\mathbb{A}_0$ is simply given by a normalisation of the diffusion tensor $\mathbb{D}_0$. Instead, if $r > 1$, then anisotropy is enhanced according to the values of the anisotropic coefficients, as given by Eq. (22).

The modification of tensors $\mathbb{D}_0$ and $\mathbb{A}_0$ is then done considering only the reorientation of the preferential directions and not their extension or compression. For this reason, the deformation gradient $\mathbb{F}_\mathrm{s}$ is used to deform the eigenvectors and the deformed eigenvectors are normalized to account only for changes in the direction (see Fig. 2). Hence, for the modified diffusion tensor we can use the expression

$$\mathbb{D} = \lambda_1^0\frac{\mathbb{F}_\mathrm{s}\mathbf{e}_1^0\otimes\mathbb{F}_\mathrm{s}\mathbf{e}_1^0}{|\mathbb{F}_\mathrm{s}\mathbf{e}_1^0|^2} + \lambda_2^0\frac{\mathbb{F}_\mathrm{s}\mathbf{e}_2^0\otimes\mathbb{F}_\mathrm{s}\mathbf{e}_2^0}{|\mathbb{F}_\mathrm{s}\mathbf{e}_2^0|^2} + \lambda_3^0\frac{\mathbb{F}_\mathrm{s}\mathbf{e}_3^0\otimes\mathbb{F}_\mathrm{s}\mathbf{e}_3^0}{|\mathbb{F}_\mathrm{s}\mathbf{e}_3^0|^2}\,,$$

where we observe that

$$\left|\mathbb{F}_\mathrm{s}\mathbf{e}_i^0\right|^2 = \mathbb{F}_\mathrm{s}\mathbf{e}_i^0\cdot\mathbb{F}_\mathrm{s}\mathbf{e}_i^0 = \mathbf{e}_i^0\cdot\mathbb{C}_\mathrm{s}\mathbf{e}_i^0\,, \quad i = 1,2,3, \quad \mathbb{C}_\mathrm{s} = \mathbb{F}_\mathrm{s}^\mathrm{T}\mathbb{F}_\mathrm{s}.$$

The preferential directions tensor $\mathbb{A}$ can be derived in a similar way to $\mathbb{D}$, i.e. deforming the eigenvectors through the deformation gradient and normalizing them:

$$\mathbb{A} = \frac{1}{\mathrm{A}_{av}}\widehat{\mathbb{A}}, \qquad \mathrm{A}_{av} = \frac{1}{3}\,\mathrm{tr}(\widehat{\mathbb{A}}),$$
$$\widehat{\mathbb{A}} = a_1^0(r)\lambda_1^0\frac{\mathbb{F}_\mathrm{s}\mathbf{e}_1^0\otimes\mathbb{F}_\mathrm{s}\mathbf{e}_1^0}{\mathbf{e}_1^0\cdot\mathbb{C}_\mathrm{s}\mathbf{e}_1^0} + a_2^0(r)\lambda_2^0\frac{\mathbb{F}_\mathrm{s}\mathbf{e}_2^0\otimes\mathbb{F}_\mathrm{s}\mathbf{e}_2^0}{\mathbf{e}_2^0\cdot\mathbb{C}_\mathrm{s}\mathbf{e}_2^0} + \lambda_3^0\frac{\mathbb{F}_\mathrm{s}\mathbf{e}_3^0\otimes\mathbb{F}_\mathrm{s}\mathbf{e}_3^0}{\mathbf{e}_3^0\cdot\mathbb{C}_\mathrm{s}\mathbf{e}_3^0}\,.$$

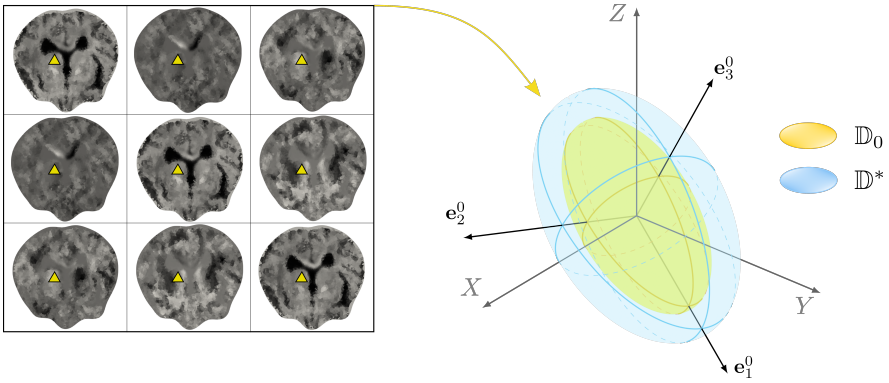


Fig. 2 Computational reconstruction and modification of the components of the diffusion tensor taken from DTI data. On the left, a sample of the six components of the initial tensor $\mathbb{D}_0$ built using medical imaging data is shown. In particular, a diffusion value is assigned to each brain mesh cell, with higher values appearing in black. For a representative cell marked by the yellow triangle, on the right we sketch the diffusion ellipsoid of the initial and modified tensors in the reference configuration. Specifically, the smaller (yellow) ellipsoid represents the preferential directions and values of diffusion at the initial time instant, i.e. the eigenvectors and eigenvalues of $\mathbb{D}_0$, respectively. The initial eigenvectors are then modified according to the deformation of the tissue to obtain the current tensor $\mathbb{D}$, as described in Section 2.1.4. In the Figure, we sketch (in blue) the pullback $\mathbb{D}^* := J_s \mathbb{F}_s^{-1} \mathbb{D} \mathbb{F}_s^{-T}$ of the modified diffusion tensor. We observe that both $\mathbb{D}_0$ and $\mathbb{D}^*$ are defined in the reference configuration and have the same eigenvectors, but different eigenvalues. For the coloured version of the Figure, we refer the reader to the online version of the Chapter.

2.1.5 Interface conditions at the boundary between the tumour and the healthy tissue

Since the material interface $\partial\Omega_t(t)$ between the tumour and the healthy tissue moves with the tumour cells with velocity $\mathbf{v}_s|_{\partial\Omega_t(t)}$, we have to satisfy the following interface conditions on the two sides of the boundary, in order to guarantee the continuity of the normal displacement, the normal stress, chemical concentration and fluxes at the interface:

$$[\![\mathbf{v}_s \cdot \mathbf{n}]\!]|_{\partial\Omega_t(t)} = 0\,, \tag{23a}$$
$$[\![\phi_\ell\,(\mathbf{v}_\ell - \mathbf{v}_s) \cdot \mathbf{n} d\Sigma]\!]|_{\partial\Omega_t(t)} = 0\,, \tag{23b}$$
$$[\![p]\!]|_{\partial\Omega_t(t)} = 0\,, \tag{23c}$$
$$[\![c_n]\!]|_{\partial\Omega_t(t)} = 0\,, \tag{23d}$$
$$[\![\mathbb{T}\mathbf{n} d\Sigma]\!]|_{\partial\Omega_t(t)} = \mathbf{0}\,, \tag{23e}$$
$$[\![(\phi_\ell c_n\,(\mathbf{v}_\ell - \mathbf{v}_s) - \phi_\ell \mathbb{D}\nabla c_n) \cdot \mathbf{n} d\Sigma]\!]|_{\partial\Omega_t(t)} = 0\,, \tag{23f}$$

where $[\![\cdot]\!]|_{\partial\Omega_t(t)}$ denotes the jump across the interface, $\mathbf{n}$ is the unit normal vector to $\partial\Omega_t(t)$ pointing outwards and $d\Sigma$ is the area element at the interface. In particular we underline that, by combining the continuity across the interface of the total stress $\mathbb{T} = -p\mathbb{I} + \mathbb{T}_s$, prescribed by Eq. (23e), and the continuity of the pressure p, prescribed

by Eq. (23c), it follows that also the effective stress $\mathbb{T}_s$ is continuous. Furthermore, due to the presence in biological tissues of cell-cell and cell-extracellular matrix adhesion molecules, it is physically reasonable to assume not only the continuity of the velocity $\mathbf{v}_s$ along the normal direction, but also that there are not breakages and rotations between the tumour and the healthy tissue. This hypothesis requires that $\mathbf{v}_s$ is continuous also along the unit tangential component $\boldsymbol{\tau}$:

$$[\![\mathbf{v}_s \cdot \boldsymbol{\tau}]\!]|_{\partial\Omega_t(t)} = 0\,.$$

This assumption leads us to say that the displacement field $\mathbf{u}_s$ is continuous along $\partial\Omega_t(t)$ and that the areas $d\Sigma$ deform in the same way at the interface, but it does not imply that also $\mathbb{F}_s$ and J_s are continuous. We observe, as well, that the cell volumetric fraction ϕ_s is in general discontinuous at the tumour interface since it is is related to the inverse of the Jacobian J_s. In the end, removing $d\Sigma$ in (23b), (23e) and (23f) for the assumption made above, the interface conditions that we impose are

$$[\![\mathbf{u}_s]\!]|_{\partial\Omega_t(t)} = \mathbf{0}\,, \tag{24a}$$
$$[\![\phi_\ell\,(\mathbf{v}_\ell - \mathbf{v}_s)\cdot\mathbf{n}]\!]|_{\partial\Omega_t(t)} = 0\,, \tag{24b}$$
$$[\![p]\!]|_{\partial\Omega_t(t)} = 0\,, \tag{24c}$$
$$[\![c_n]\!]|_{\partial\Omega_t(t)} = 0\,, \tag{24d}$$
$$[\![\mathbb{T}_s\mathbf{n}]\!]|_{\partial\Omega_t(t)} = \mathbf{0}\,, \tag{24e}$$
$$[\![(\phi_\ell c_n\,(\mathbf{v}_\ell - \mathbf{v}_s) - \phi_\ell\mathbb{D}\nabla c_n)\cdot\mathbf{n}]\!]|_{\partial\Omega_t(t)} = 0\,. \tag{24f}$$

2.2 Lagrangian formulation of the model

To approach the numerical implementation of the model, our aim is to rewrite the equations derived in Section 2.1 using a Lagrangian description of motion. In this way, all the quantities of interest are considered in terms of material coordinates. Henceforth, we will then use a superscript * to denote any material element. Furthermore, we will use the same symbols to denote the variables in the spatial and material description, omitting the explicit spatial dependence. We recall the following equalities, which will be useful in the successive computations:

$$d\Sigma = J_s\mathbb{F}_s^{-T}d\Sigma^*, \qquad dV = J_s dV^*\,, \tag{25}$$

where $d\Sigma = \mathbf{n}d\Sigma$ and dV represent the infinitesimal element of area and volume in spatial coordinates, respectively, $d\Sigma^* = \mathbf{N}d\Sigma^*$ and dV^* denote the infinitesimal element of area and volume in material coordinates, while $\mathbf{N}$ denotes the unit normal vector to $\partial\Omega_t^*$ pointing outwards [45].
Firstly, we integrate Equation (3) for $\alpha = s$ over the tumour domain $\Omega_t(t)$ to obtain

$$\int_{\Omega_{t(t)}}\left[\frac{\partial\phi_s}{\partial t} + \nabla\cdot(\phi_s\mathbf{v}_s)\right]dV = \int_{\Omega_{t(t)}}\Gamma_s\,dV\,.$$

Using Reynolds' transport theorem, see for example [45], and moving the volume elements to the reference configuration by means of (25), we obtain

$$\frac{d}{dt}\int_{\Omega_t^*} \phi_s J_s \, dV^* = \int_{\Omega_t^*} \Gamma_s J_s \, dV^* ,$$

which locally becomes

$$\dot{\overline{J_s \phi_s}} = J_s \Gamma_s . \tag{26}$$

For what concerns Equation (3) for $\alpha = \ell$, integrating over the tumour domain gives

$$\int_{\Omega_{t(t)}} \left[\frac{\partial \phi_\ell}{\partial t} + \nabla \cdot (\phi_\ell \mathbf{v}_\ell) \right] dV = - \int_{\Omega_{t(t)}} \Gamma_s \, dV .$$

Since the interface does not move with the fluid, we have to make use of the generalized Reynolds' transport theorem [45] which, together with the divergence theorem and Eq. (25), yields

$$\frac{d}{dt}\int_{\Omega_t^*} \phi_\ell J_s \, dV^* - \int_{\Omega_t^*} \mathrm{Div}\left[J_s \phi_\ell \mathbb{F}_s^{-1} (\mathbf{v}_s - \mathbf{v}_\ell) \right] dV^* = - \int_{\Omega_t^*} \Gamma_s J_s \, dV^* ,$$

which localized gives

$$\dot{\overline{J_s \phi_\ell}} + \mathrm{Div}\left[J_s \phi_\ell \mathbb{F}_s^{-1} (\mathbf{v}_\ell - \mathbf{v}_s) \right] = -\Gamma_s J_s . \tag{27}$$

Then, if we recall that ϕ_{sn} is the volumetric fraction in the natural state and it is a constant quantity, using (15) we can rewrite (26) as

$$J_s \phi_s = J_g \phi_{sn} \quad \Rightarrow \quad J_s \phi_s = g^3 \phi_{sn} .$$

As regards the momentum balance of the solid phase, if we integrate (9) over the tumour domain and we remember that $\mathbb{T} = -p\mathbb{I} + \mathbb{T}_s$ is the Cauchy stress tensor of the mixture, we obtain

$$\int_{\Omega_{t(t)}} \nabla \cdot \mathbb{T} \, dV = \mathbf{0} .$$

Introducing the first Piola-Kirchhoff stress tensor $\mathbb{P} := J_s \mathbb{T} \mathbb{F}_s^{-\mathrm{T}}$, the latter becomes

$$\int_{\Omega_t^*} \mathrm{Div}\, \mathbb{P} \, dV^* = \mathbf{0} \quad \Longrightarrow \quad \mathrm{Div}\, \mathbb{P} = \mathbf{0} .$$

Recalling that $\mathbb{P} = J_s \mathbb{T} \mathbb{F}_s^{-\mathrm{T}} = -J_s p \mathbb{F}_s^{-\mathrm{T}} + \mathbb{P}_s$, we have

$$\mathrm{Div}\left[-J_s p \mathbb{F}_s^{-\mathrm{T}} + \mathbb{P}_s \right] = \mathbf{0} .$$

In order to rewrite (10) using the Lagrangian formulation, we integrate over a surface

$$\int_S \phi_\ell \left(\mathbf{v}_\ell - \mathbf{v}_\mathrm{s}\right) \cdot d\Sigma = -\int_S \frac{\mathbb{K}(\phi_\ell)}{\mu} \nabla p \cdot d\Sigma \,.$$

Moving the integrals to the reference configuration, we get

$$\int_{S^*} \left[\frac{\mathbb{K}}{\mu} \mathbb{F}_\mathrm{s}^{-\mathrm{T}} \operatorname{Grad} p + \phi_\ell \left(\mathbf{v}_\ell - \mathbf{v}_\mathrm{s}\right)\right] \cdot J_\mathrm{s} \mathbb{F}_\mathrm{s}^{-\mathrm{T}} d\boldsymbol{\Sigma}^* = 0 \,.$$

Let us assume that all the involved quantities are regular, we have then the local form

$$\mathbf{v}_\ell - \mathbf{v_s} = -\mathbb{F}_\mathrm{s} \frac{\mathbb{K}^*}{J_\mathrm{s} \mu \phi_\ell} \operatorname{Grad} p \,, \tag{28}$$

defining the tensor pullback $\mathbb{K}^* := J_\mathrm{s} \mathbb{F}_\mathrm{s}^{-1} \mathbb{K} \mathbb{F}_\mathrm{s}^{-\mathrm{T}}$.
In the light of Eq. (28), it is then convenient to further reformulate the mass balances by summing up Eqs. (26) and (27). Using the saturation condition and the closed mixture assumption, the mass balance for the mixture therefore reads

$$\dot{J}_\mathrm{s} = \operatorname{Div}\left[\frac{\mathbb{K}^*}{\mu} \operatorname{Grad} p\right] .$$

Referring to the nutrients balance equation (21a), integrating it over the tumour domain and recalling the closed mixture assumption, we obtain

$$\int_{\Omega_{\mathrm{t}(t)}} \left[\frac{\partial \left(\phi_\ell c_n\right)}{\partial t} + \nabla \cdot \left(\phi_\ell c_n \mathbf{v}_\ell\right)\right] dV = \int_{\Omega_{\mathrm{t}(t)}} \nabla \cdot \left(\phi_\ell \mathbb{D} \nabla c_n\right) dV - \int_{\Omega_{\mathrm{t}(t)}} \left(\Gamma_\mathrm{s} c_n - G_n\right) dV \,,$$

that localized by means of the generalized Reynolds' transport theorem and the Gauss theorem leads to

$$\dot{\overline{J_\mathrm{s} \phi_\ell c_n}} - \operatorname{Div}\left[J_\mathrm{s} \phi_\ell c_n \mathbb{F}_\mathrm{s}^{-1} \left(\mathbf{v}_\mathrm{s} - \mathbf{v}_\ell\right)\right] - \operatorname{Div}\left[J_\mathrm{s} \phi_\ell \mathbb{F}_\mathrm{s}^{-1} \mathbb{D} \mathbb{F}_\mathrm{s}^{-\mathrm{T}} \operatorname{Grad} c_n\right] = - \Gamma_\mathrm{s} c_n J_\mathrm{s} + G_n J_\mathrm{s} \,.$$

If we define $\mathbb{D}^* := J_\mathrm{s} \mathbb{F}_\mathrm{s}^{-1} \mathbb{D} \mathbb{F}_\mathrm{s}^{-\mathrm{T}}$ and we recall the mass balance of the fluid phase (27), substituting Darcy's law in the reference configuration (28) we can rewrite it as

$$J_\mathrm{s} \phi_\ell \dot{c}_n - \frac{\mathbb{K}^*}{\mu} \operatorname{Grad} p \cdot \operatorname{Grad} c_n - \operatorname{Div}\left[\phi_\ell \mathbb{D}^* \operatorname{Grad} c_n\right] = J_\mathrm{s} G_n \,. \tag{29}$$

In conclusion, the set of equations in Lagrangian form in the tumour reference domain Ω_t^* is

$$\dot{J}_\mathrm{s} = \mathrm{Div}\left[\frac{\mathbb{K}^*}{\mu}\,\mathrm{Grad}\,p\right], \tag{30a}$$

$$\phi_\mathrm{s} = J_\mathrm{s}^{-1} g^3 \phi_\mathrm{sn}, \tag{30b}$$

$$\phi_\mathrm{s} + \phi_\ell = 1, \tag{30c}$$

$$\mathrm{Div}\left[-J_\mathrm{s} p \mathbb{F}_\mathrm{s}^{-\mathrm{T}} + \mathbb{P}_\mathrm{s}\right] = \mathbf{0}, \tag{30d}$$

$$\frac{\dot{g}}{g} = \frac{1}{3}\frac{\Gamma_\mathrm{s}}{\phi_\mathrm{s}}, \tag{30e}$$

$$J_\mathrm{s}\phi_\ell \dot{c}_n - \frac{\mathbb{K}^*}{\mu}\,\mathrm{Grad}\,p \cdot \mathrm{Grad}\,c_n - \mathrm{Div}\left[\phi_\ell \mathbb{D}^*\,\mathrm{Grad}\,c_n\right] = J_\mathrm{s} G_n\,. \tag{30f}$$

A similar reasoning and analogous computations can be used to derive the Lagrangian equations in the healthy tissue reference domain, so that we end up with the following set of equations in Ω_h^*

$$\dot{J}_\mathrm{s} = \mathrm{Div}\left[\frac{\mathbb{K}^*}{\mu}\,\mathrm{Grad}\,p\right], \tag{31a}$$

$$\phi_\mathrm{s} = J_\mathrm{s}^{-1} g^3 \phi_\mathrm{sn}, \tag{31b}$$

$$\phi_\mathrm{s} + \phi_\ell = 1, \tag{31c}$$

$$\mathrm{Div}\left[-J_\mathrm{s} p \mathbb{F}_\mathrm{s}^{-\mathrm{T}} + \mathbb{P}_\mathrm{s}\right] = \mathbf{0}, \tag{31d}$$

$$\dot{g} = 0, \tag{31e}$$

$$J_\mathrm{s}\phi_\ell \dot{c}_n - \frac{\mathbb{K}^*}{\mu}\,\mathrm{Grad}\,p \cdot \mathrm{Grad}\,c_n - \mathrm{Div}\left[\phi_\ell \mathbb{D}^*\,\mathrm{Grad}\,c_n\right] = 0\,. \tag{31f}$$

The systems (30) and (31) allow to determine all the unknown fields, namely, the displacement field $\mathbf{u}_\mathrm{s}(\mathbf{X},t)$ and the scalar fields $p(\mathbf{X},t)$, $\phi_\mathrm{s}(\mathbf{X},t)$, $\phi_\ell(\mathbf{X},t)$, $g(\mathbf{X},t)$ and $c_n(\mathbf{X},t)$, $\forall \mathbf{X} \in \Omega^* = \Omega_\mathrm{t}^* \cup \Omega_\mathrm{h}^*$ and $\forall t \in (0,T)$, if we provide proper interface, initial and boundary conditions.

Interface conditions. The interface conditions derived in Section 2.1.5, i.e. Eqs. (24a)-(24f), need to be reformulated in Lagrangian coordinates, by making use of the relations (25). Then, the set of interface conditions we obtain are the following:

$$[\![\mathbf{u}_\mathrm{s}]\!]|_{\partial\Omega_\mathrm{t}^*} = \mathbf{0}, \tag{32a}$$

$$[\![\frac{\mathbb{K}^*}{\mu}\,\mathrm{Grad}\,p \cdot \mathbf{N}]\!]|_{\partial\Omega_\mathrm{t}^*} = 0, \tag{32b}$$

$$[\![\mathbb{P}_\mathrm{s}\mathbf{N}]\!]|_{\partial\Omega_\mathrm{t}^*} = \mathbf{0}, \tag{32c}$$

$$[\![p]\!]|_{\partial\Omega_\mathrm{t}^*} = 0, \tag{32d}$$

$$[\![c_n]\!]|_{\partial\Omega_\mathrm{t}^*} = 0, \tag{32e}$$

$$[\![\,\phi_\ell \mathbb{D}^*\,\mathrm{Grad}\,c_n \cdot \mathbf{N}]\!]|_{\partial\Omega_\mathrm{t}^*} = 0\,. \tag{32f}$$

Boundary conditions. Before imposing the boundary conditions, it is important to remark that $\partial\Omega^*_{\mathrm{h}} = \partial\Omega^*_{\mathrm{t}} \cup \partial\Omega^*_{\mathrm{out}}$ is the boundary of the healthy domain that is composed by the interface with the tumour $\partial\Omega^*_{\mathrm{t}}$ and by the external boundary corresponding to the cranial skull $\partial\Omega^*_{\mathrm{out}}$. In our simulations for tumour growth in the brain, we consider the following boundary conditions on $\partial\Omega^*_{\mathrm{out}}$:

$$\mathbf{u}_{\mathrm{s}} = \mathbf{0} \qquad \text{on } \partial\Omega^*_{\mathrm{out}}\,, \quad \forall t \in (0,T)\,, \tag{33a}$$

$$p = 0 \qquad \text{on } \partial\Omega^*_{\mathrm{out}}\,, \quad \forall t \in (0,T)\,, \tag{33b}$$

$$c_n = 1 \qquad \text{on } \partial\Omega^*_{\mathrm{out}}\,, \quad \forall t \in (0,T)\,. \tag{33c}$$

We impose a null Dirichlet boundary condition for the displacement $\mathbf{u}_{\mathrm{s}}$ and for the pressure p. For the nutrients concentration we suppose that the brain boundary is sufficiently far from the tumour. Therefore, we can assume that, on the boundary, the oxygen concentration is maintained constant at the physiological value of 1 by the vasculature. When the tumour grows close to the boundary, the boundary conditions proposed in [62] should be applied.

Initial conditions. At the beginning of the tumour growth process we assume that the displacement and the pressure are equal to zero. Furthermore, we take the scalar field g, related to the growth component of the deformation gradient, as equal to 1 everywhere in the domain at $t = 0$. We also assume that the volumetric fraction of the cell phase is initially equal to the constant volumetric fraction in the natural state ϕ_{sn}. Finally, in order to obtain the initial nutrients concentration $c_n^0(\mathbf{X})$, we solve the steady version of the nutrients governing equation, neglecting advection:

$$-\operatorname{Div}\left[\phi_\ell \mathbb{D}_0 \operatorname{Grad} c_n\right] = J_{\mathrm{s}} G_n\,.$$

In conclusion, we have the following set of initial conditions:

$$\begin{aligned}
\mathbf{u}_{\mathrm{s}}(\mathbf{X},0) &= \mathbf{0} && \forall \mathbf{X} \in \Omega^*\,,\\
p(\mathbf{X},0) &= 0 && \forall \mathbf{X} \in \Omega^*\,,\\
g(\mathbf{X},0) &= 1 && \forall \mathbf{X} \in \Omega^*\,,\\
\phi_{\mathrm{s}}(\mathbf{X},0) &= \phi_{\mathrm{sn}} && \forall \mathbf{X} \in \Omega^*\,,\\
c_n(\mathbf{X},0) &= c_n^0(\mathbf{X}) && \forall \mathbf{X} \in \Omega^*\,.
\end{aligned}$$

3 Numerical implementation

In this Section, we discuss how the Lagrangian model for brain tumour growth, equipped with proper boundary and initial conditions, is solved through numerical simulations. First of all, we derive the weak formulation of the Lagrangian model. Then, we discretise in time and space the weak formulation and we assess the values

of the parameters that appear in the system. Finally, we describe how we manage to generate the patient-specific mesh that has been used for the computation.

3.1 Weak formulation of the Lagrangian model

We will derive now a weak formulation of our Lagrangian model. We first write the weak form in each domain Ω_t^* and Ω_h^* separately and then we extend the weak form to the whole domain $\Omega^* = \Omega_\mathrm{t}^* \cup \Omega_\mathrm{h}^*$. At this point, we define the test functions space that meets the Dirichlet conditions we impose on the external boundary for p (33b) and c_n (33c), recalling that p and c_n are continuous functions over Ω^*:

$$H^1_{0,\partial\Omega^*_\mathrm{out}}(\Omega^*) := \left\{ q \in H^1(\Omega^*) \colon q = 0 \text{ on } \partial\Omega^*_\mathrm{out} \right\} .$$

Furthermore, we establish the vector test functions space that meets the Dirichlet conditions we impose on the external boundary for the continuous vector function $\mathbf{u}_\mathrm{s}$ (33a):

$$\boldsymbol{H}^1_{0,\partial\Omega^*_\mathrm{out}}(\Omega^*) := \left\{ \boldsymbol{q} \in \boldsymbol{H}^1(\Omega^*) \colon \boldsymbol{q} = \mathbf{0} \text{ on } \partial\Omega^*_\mathrm{out} \right\} .$$

Then, starting from Eq. (30a), we multiply each side by a test function $q_\mathrm{t} \in H^1_{0,\partial\Omega^*_\mathrm{out}}(\Omega^*)$ and we integrate the whole equation over the Lagrangian tumour domain:

$$\int_{\Omega_\mathrm{t}^*} \dot{J}_\mathrm{s} q_\mathrm{t} \, dV^* = \int_{\Omega_\mathrm{t}^*} \mathrm{Div}\left[\frac{\mathbb{K}^*}{\mu} \mathrm{Grad}\, p \right] q_\mathrm{t} \, dV^* .$$

Integrating by parts the second order derivatives, we obtain

$$\int_{\Omega_\mathrm{t}^*} \dot{J}_\mathrm{s} q_\mathrm{t} \, dV^* = -\int_{\Omega_\mathrm{t}^*} \mathrm{Grad}\, q_\mathrm{t} \cdot \frac{\mathbb{K}^*}{\mu} \mathrm{Grad}\, p \, dV^* + \int_{\partial\Omega_\mathrm{t}^*} q_\mathrm{t} \frac{\mathbb{K}^*}{\mu} \mathrm{Grad}\, p \cdot \mathbf{N} d\Sigma^* .$$

In the healthy domain we take as test function $q_\mathrm{h} \in H^1_{0,\partial\Omega^*_\mathrm{out}}(\Omega^*)$ and we find

$$\int_{\Omega_\mathrm{h}^*} \dot{J}_\mathrm{s} q_\mathrm{h} \, dV^* = -\int_{\Omega_\mathrm{h}^*} \mathrm{Grad}\, q_\mathrm{h} \cdot \frac{\mathbb{K}^*}{\mu} \mathrm{Grad}\, p \, dV^* + \int_{\partial\Omega_\mathrm{t}^*} q_\mathrm{h} \frac{\mathbb{K}^*}{\mu} \mathrm{Grad}\, p \cdot \mathbf{N} d\Sigma^* ,$$

since the test function q_h is required to vanish on the boundary $\partial\Omega^*_\mathrm{out}$ because it belongs to $H^1_{0,\partial\Omega^*_\mathrm{out}}(\Omega^*)$. Summing up the equations in the healthy and tumour domain taking $q \in H^1_{0,\partial\Omega^*_\mathrm{out}}(\Omega^*)$ we have

$$\int_{\Omega^*} \dot{J}_\mathrm{s} q \, dV^* = -\int_{\Omega^*} \mathrm{Grad}\, q \cdot \frac{\mathbb{K}^*}{\mu} \mathrm{Grad}\, p \, dV^* - \int_{\partial\Omega_\mathrm{t}^*} \left[\!\left[q \frac{\mathbb{K}^*}{\mu} \mathrm{Grad}\, p \right]\!\right] \cdot \mathbf{N} d\Sigma^* .$$

Since the test function q belongs to $H^1_{0,\partial\Omega^*_\mathrm{out}}(\Omega^*)$ and so it is continuous inside the domain, thanks to interface condition (32b) we finally have

$$\int_{\Omega^*} \dot{J}_s q \, dV^* = -\int_{\Omega^*} \text{Grad}\, q \cdot \frac{\mathbb{K}^*}{\mu} \text{Grad}\, p \, dV^* , \tag{34}$$

for all test functions $q \in H^1_{0,\partial\Omega^*_{\text{out}}}(\Omega^*)$.
For what concerns the momentum balance, we multiply (30d) by a vector test function $\boldsymbol{q}_t \in \boldsymbol{H}^1_{0,\partial\Omega^*_{\text{out}}}(\Omega^*)$ and then we integrate over the tumour reference domain, obtaining

$$\int_{\Omega^*_t} \text{Div}\left[-J_s p \mathbb{F}_s^{-T} + \mathbb{P}_s\right] \cdot \boldsymbol{q}_t \, dV^* = 0 .$$

Using tensor integration by parts, we get

$$-\int_{\Omega^*_t} \left(-J_s p \mathbb{F}_s^{-T} + \mathbb{P}_s\right) : \text{Grad}\, \boldsymbol{q}_t \, dV^* + \int_{\partial\Omega^*_t} \left(-J_s p \mathbb{F}_s^{-T} + \mathbb{P}_s\right) \mathbf{N} \cdot \boldsymbol{q}_t \, d\Sigma^* = 0 .$$

If we do the same in the healthy domain and sum the two equations, with $\boldsymbol{q} \in \boldsymbol{H}^1_{0,\partial\Omega^*_{\text{out}}}(\Omega^*)$, the weak formulation on the whole domain is

$$-\int_{\Omega^*} \left(-J_s p \mathbb{F}_s^{-T} + \mathbb{P}_s\right) : \text{Grad}\, \boldsymbol{q} \, dV^* - \int_{\partial\Omega^*_t} \left[\!\left[\left(-J_s p \mathbb{F}_s^{-T} + \mathbb{P}_s\right) \mathbf{N} \cdot \boldsymbol{q}\right]\!\right] d\Sigma^* = 0 .$$

Recalling that the displacement is taken continuous in all directions (32a), the areas deform in the same way at the interface. For this reason, the first relation in (25) implies $[\![J_s \mathbb{F}_s^{-T} \mathbf{N}]\!]|_{\partial\Omega^*_t} = \mathbf{0}$. Looking at this condition and at the interface conditions (32c) and (32d), recalling that $\boldsymbol{q} \in \boldsymbol{H}^1_{0,\partial\Omega^*_{\text{out}}}(\Omega^*)$, the jump vanishes and we are left with

$$-\int_{\Omega^*} \left(-J_s p \mathbb{F}_s^{-T} + \mathbb{P}_s\right) : \text{Grad}\, \boldsymbol{q} \, dV^* = 0 . \tag{35}$$

We need then a weak formulation for the equation of the nutrients. In order to derive it, we multiply (30f) by a test function $q_t \in H^1_{0,\partial\Omega^*_{\text{out}}}(\Omega^*)$ and we integrate by parts, obtaining

$$\int_{\Omega^*_t} \left(J_s \phi_\ell \dot{c}_n - \frac{\mathbb{K}^*}{\mu} \text{Grad}\, p \cdot \text{Grad}\, c_n\right) q_t \, dV^* + \int_{\Omega^*_t} \phi_\ell \, \text{Grad}\, q_t \cdot \mathbb{D}^* \, \text{Grad}\, c_n \, dV^* +$$
$$- \int_{\partial\Omega^*_t} q_t \phi_\ell \mathbb{D}^* \, \text{Grad}\, c_n \cdot \mathbf{N} d\Sigma^* = \int_{\Omega^*_t} J_s G_n q_t \, dV^* .$$

We follow the same approach in the healthy domain and then we sum the two equations. Taking $q \in H^1_{0,\partial\Omega^*_{\text{out}}}(\Omega^*)$, the test function vanishes on the external boundary and, recalling the interface condition (32f), we finally have

$$\int_{\Omega^*}\left(J_s\phi_\ell\dot{c}_n-\frac{\mathbb{K}^*}{\mu}\operatorname{Grad}p\cdot\operatorname{Grad}c_n\right)q\,dV^*+\int_{\Omega^*}\phi_\ell\operatorname{Grad}q\cdot\mathbb{D}^*\operatorname{Grad}c_n\,dV^*=$$
$$=\int_{\Omega^*}J_sG_nq\,dV^*\,. \quad (36)$$

We remark that, given the pressure p and the displacement $\mathbf{u}_s$ obtained by solving (34) and (35), Eq. (36) represents a linear variational problem to be solved for the unknown c_n.

3.2 Discrete formulation of the continuous variational problems

We need now to introduce a time and spatial discrete formulation of the continuous variational problems (34), (35) and (36). We make use of linear tetrahedron $\mathbb{P}_1$ elements, so we introduce the following finite element spaces:

$$\boldsymbol{V}_h:=\left\{\boldsymbol{q}_h\in\left[C^0\left(\overline{\Omega^*}\right)\right]^3:\boldsymbol{q}_h|_K\in[\mathbb{P}_1(K)]^3\ \forall K\in\mathcal{T}_h,\ \boldsymbol{q}_h=\mathbf{0}\text{ on }\partial\Omega^*_{\text{out}}\right\}\subset\boldsymbol{H}^1_{0,\partial\Omega^*_{\text{out}}}(\Omega^*)\,,$$
$$W_{h0}:=\left\{q_h\in C^0\left(\overline{\Omega^*}\right):q_h|_K\in\mathbb{P}_1(K)\,\forall K\in\mathcal{T}_h,\ q_h=0\text{ on }\partial\Omega^*_{\text{out}}\right\}\subset H^1_{0,\partial\Omega^*_{\text{out}}}(\Omega^*)\,,$$
$$W_{h1}:=\left\{q_h\in C^0\left(\overline{\Omega^*}\right):q_h|_K\in\mathbb{P}_1(K)\,\forall K\in\mathcal{T}_h,\ q_h=1\text{ on }\partial\Omega^*_{\text{out}}\right\}\subset H^1(\Omega^*)\,,$$

where $\mathcal{T}_h$ is a decomposition of the domain Ω^* into tetrahedra K conforming to the tumour boundary.
For what concerns the time discretization, given N time instants on the interval $(0,T)$, $\Delta t:=T/N$ is the time step and we use a superscript k to denote the value of a quantity at time $t_k=k\Delta t$. In order to simplify the notation, we will drop the superscript $k+1$ to denote the value of a quantity of interest at the next time step.
Then, we can define the full discrete variational problem, summing (34) and (35) to rewrite them into a single nonlinear variational problem.
Thus, we can formulate the problem as follows

for $k=1,...,N$, given $\left(\mathbf{u}_h^k,p_h^k,c_h^k\right)\in\boldsymbol{V}_h\times W_{h0}\times W_{h1}$ find $(\mathbf{u}_h,p_h,c_h)\in\boldsymbol{V}_h\times W_{h0}\times W_{h1}$ such that $\forall(\boldsymbol{v}_h,w_h,q_h)\in\boldsymbol{V}_h\times W_{h0}\times W_{h0}$ it holds

$$\left(J_s(\mathbf{u}_h),w_h\right)+\Delta t\left(\operatorname{Grad}w_h,\frac{\mathbb{K}^*}{\mu}\operatorname{Grad}p_h\right)-\left(\mathbb{P}(\mathbf{u}_h,p_h),\operatorname{Grad}\boldsymbol{v}_h\right)=\left(J_s^k\left(\mathbf{u}_h^k\right),w_h\right),$$
$$\left(J_s(\mathbf{u}_h)c_h,q_h\right)-\Delta t\left(\frac{\mathbb{K}^*}{\mu\phi_\ell}\operatorname{Grad}p_h\cdot\operatorname{Grad}c_h,q_h\right)+\Delta t\left(\operatorname{Grad}q_h,\mathbb{D}^*\operatorname{Grad}c_h\right)=$$
$$=\left(J_s(\mathbf{u}_h)c_h^k,q_h\right)+\Delta t\left(J_s(\mathbf{u}_h)\frac{G_n(c_h)}{\phi_\ell},q_h\right),$$

where for simplicity we have denoted by $(\cdot,\cdot)$ the standard scalar product on the spaces $L^2(\Omega^*)$, $L^2(\Omega^*;\mathbb{R}^3)$ and $L^2(\Omega^*;\mathbb{R}^{3\times3})$ when appropriate.

The last step is to introduce a proper discretisation of the other equations involved, namely the ordinary differential equation for g (17), the saturation condition (30c) and the relation (30b). Let g_h, $\phi_{\mathrm{s},h}$ and $\phi_{\ell,h}$ be piecewise-constant functions approximating g, ϕ_{s} and ϕ_ℓ, respectively. Regarding (17), it can be discretised in time using the explicit Euler method, only in the nodes which belong to the tumour domain Ω_{t}^*:

$$g_h = g_h^k \left(1 + \Delta t \frac{\Gamma_{\mathrm{s}}(c_h^k, \phi_{\mathrm{s},h}^k)}{3\phi_{\mathrm{s},h}^k}\right).$$

Equation (30b) is discretized as

$$\phi_{\mathrm{s},h} = J_{\mathrm{s}}^{-1}(\mathbf{u}_h) g_h^3 \phi_{\mathrm{sn}}.$$

Once we have computed $\phi_{\mathrm{s},h}$, we can derive $\phi_{\ell,h}$ using the saturation condition

$$\phi_{\ell,h} = 1 - \phi_{\mathrm{s},h}.$$

Furthermore, a time-step control was made, which allows us to ensure the convergence of the numerical simulation.

3.3 Parameters estimation

Before performing numerical simulations, we have to assess the values of the parameters that appear in the system. It is important to remark that the choice of the parameters is fundamental to have a realistic outcome for the model. On the other hand, when working in the field of mathematical biomedicine, it is often difficult to have precise estimations of the parameters involved. In this Section, we review the literature in order to assign a value or a range of admissible values to the parameters introduced in our model.

Firstly, we deal with the mechanical parameters $\mu_{1\mathrm{h}}$ and $\mu_{2\mathrm{h}}$ that appear in the Mooney-Rivlin energy density for the healthy tissue. In the article of Balbi et al. [13], the authors propose as mean values for the material parameters $\mu_{1\mathrm{h}} = 3.06 \cdot 10^{-4}$ MPa and $\mu_{2\mathrm{h}} = 5.94 \cdot 10^{-4}$ MPa, which we choose as references. For what concerns instead the Mooney-Rivlin parameters in the diseased tissue, we will consider them as ten times greater than the healthy ones, that means $\mu_{1\mathrm{t}} = 3.06 \cdot 10^{-3}$ MPa and $\mu_{2\mathrm{t}} = 5.94 \cdot 10^{-3}$ MPa.

The volumetric moduli κ_{t} and κ_{h} penalise volumetric changes in the solid skeleton. Unfortunately, it is difficult to estimate their numerical value, since in the majority of the works available in the literature, both on the experimental and on the modelling sides, the brain is not considered as a mixture. We take as a reference the work by Prevost et al. [74], who estimate a range of $2 \cdot 10^2 - 2 \cdot 10^4$ Pa for the volumetric modulus. Therefore, taking into account that the brain is very soft, we choose $\kappa_{\mathrm{t}} = 1.389 \cdot 10^{-3}$ MPa and $\kappa_{\mathrm{h}} = 1.389 \cdot 10^{-4}$ MPa.

Then, we have to provide values of the parameters involved in the growth rate Γ_{s}

proposed in Eq. (18). The growth parameter ν is estimated using typical proliferation times for glioma cells *in vitro*, which range between 24–48 hours: this corresponds to values of $0.5 - 1$ day^{-1}. As underlined in [24,62], proliferation is strongly affected by the availability of nutrients, allowing also smaller values to be appropriate for ν. Having said that, in the following we will fix a value of $\nu = 0.5$ day^{-1}. For what concerns the maximum cell volume fraction $\phi_{\max}$, since we are not modelling the formation of calcifications and necrotic regions, we assume that a minimum amount of extracellular liquid is always present in the tissue to keep cells alive. Consequently, $\phi_{\max} < 1$. In the numerical simulations we set $\phi_{\max} = 0.95$.
The values for the hypoxia threshold c_0 which are found in the literature [1,40,41,90] are quite different and cover a range from 0.15 to 0.5. We will consider $c_0 = 0.30$ in simulations, as done by Agosti et al. in [1]. Concerning the nutrients consumption rate ζ that appears in Eq. (20), we follow the approach by Colombo et al. [24] and so we know it can be estimated as $\zeta = 8640$ day^{-1}. For the estimation of the nutrients supply rate S_n, we rely on the value of 10^4 day^{-1} proposed in [20], as done also in [1, 24]. We need then to give an estimate of the cell volumetric fraction in the natural state ϕ_{sn}, which is a constant given from the outset. Specifically, we consider a value of $\phi_{\text{sn}} = 0.40$, in accordance with the fact that the extra-cellular space, which is complementary to the solid volume fraction, amounts approximately at 61% [18]. It is also necessary to introduce and estimate the function $K(\phi_\ell)$ which appears in the permeability tensor expression (11). For the saturation condition (1), it can be equivalently expressed as a function of ϕ_{s}. As a functional form for such a permeability function, we will consider the exponential Holmes-Mow expression [51], which is frequently used in the modelling of soft tissues [28]

$$K(\phi_\ell) = \tilde{K}(\phi_{\text{s}}) = k_0 \left[\frac{\phi_{\text{sn}}(1-\phi_{\text{s}})}{\phi_{\text{s}}(1-\phi_{\text{sn}})} \right]^{\alpha_0} e^{\frac{m}{2}\left(\frac{\phi_{\text{sn}}^2 - \phi_{\text{s}}^2}{\phi_{\text{s}}^2}\right)},$$

in which α_0 and m are model parameters, whereas k_0 is a reference permeability value taken in the natural state. In particular, for what concerns the value of k_0, in the literature it is often estimated the ratio $k_{\text{c}} := \frac{k_0}{\mu}$, where μ is the dynamic viscosity of the fluid phase. Following this definition and given the spatial and temporal scales of our model, such a ratio has units mm^2/(MPa $\cdot$ day). Values found in the literature cover quite a wide range: Mascheroni et al. [68] consider a value of $4.2 \cdot 10^4$ mm^2/(MPa $\cdot$ day) for the fluid phase in a mixture model for brain tumour spheroids. On the other hand, the values $4.31 \cdot 10^5 - 6.47 \cdot 10^5$mm^2/(MPa $\cdot$ day) were proposed by Basser [15] for the permeability of white and grey matter, respectively. We consider an intermediate value, that corresponds to $k_{\text{c}} = 2.17 \cdot 10^5$ mm^2/(MPa $\cdot$ day), as done also in [62]. Furthermore, the values $\alpha_0 = 0.0848$ and $m = 4.638$ are considered, as it is usually done for the Holmes-Mow permeability in soft tissues [28]. In Table 2 we report the complete list of all the used parameters, together with the values employed in the simulations.

Parameter	Description	Value
μ_{1h}	Mooney-Rivlin material parameter (healthy)	$3.06 \cdot 10^{-4}$ MPa
μ_{2h}	Mooney-Rivlin material parameter (healthy)	$5.94 \cdot 10^{-4}$ MPa
μ_{1t}	Mooney-Rivlin material parameter (tumour)	$3.06 \cdot 10^{-3}$ MPa
μ_{2t}	Mooney-Rivlin material parameter (tumour)	$5.94 \cdot 10^{-3}$ MPa
κ_h	Volumetric modulus (healthy)	$1.389 \cdot 10^{-4}$ MPa
κ_t	Volumetric modulus (tumour)	$1.389 \cdot 10^{-3}$ MPa
ν	Cell proliferation constant	0.5 day^{-1}
c_0	Hypoxia threshold	0.30
ζ	Nutrients consumption rate	8640 day^{-1}
S_n	Nutrients supply rate	10^4 day^{-1}
ϕ_{sn}	Cell volume fraction in the natural state	0.40
ϕ_{max}	Maximum cell volume fraction	0.95
k_c	Hydraulic conductivity	$2.17 \cdot 10^5$ mm$^2 \cdot$MPa$^{-1} \cdot$day^{-1}
α_0	Holmes-Mow permeability parameter	0.0848
m	Holmes-Mow permeability parameter	4.638

Table 2 List of the values of the model parameters employed in the numerical simulations.

3.4 Mesh preparation

The last step needed to perform the numerical simulations is the introduction of the computational brain mesh, containing the values of $\mathbb{D}_0$ and, consequently, the values of $\mathbb{A}_0$. The mesh was constructed using the Magnetic Resonance Imaging (MRI) data of a single patient, acquired in the context of normal clinical practice by the Istituto Neurologico Carlo Besta in Milan (Italy). The main advantages of MRI lie in its efficiency in detecting brain tumours and its capability to highlight the different tissue types composing the brain. Nevertheless, MRI does not provide any information concerning the micro-structural architecture of the brain and the preferential direction of water diffusion. Therefore, the values of $\mathbb{D}_0$ should be derived from Diffusion Tensor Imaging (DTI) data. In this technique the water diffusivity within each voxel of the brain is described through a symmetric and positive definite tensor, whose diagonal elements are proportional to the apparent diffusivity along the three measurement directions, while the other elements are the correlation terms between molecular displacements in directions perpendicular to the measurement direction at a given time. The capacity of DTI to determine the anisotropic diffusion of water molecules provides a way to identify and visualise the orientation of white matter tracts and, consequently, the direction of cell migration.

First, we performed the segmentation of MRI grey-scale images, i.e. the partitioning into several image segments, by assigning a label to every pixel in order to reconstruct the boundary of the brain and eventually distinguish different brain tissues. This can be done using specific software packages, such as *Slicer3D* [79]. Once the segmentation has been performed, the computational mesh was constructed using *Tetgen* [46], which is able to generate tetrahedral meshes of any 3D polyhedral domain. This software enables us to construct a tumour-conformal mesh, in order to

clearly separate the healthy domain from the tumour domain. In the present work, this latter is built as a sphere of radius 7 mm located in the healthy tissue of the patient, in order to use DTI data that are not corrupted by the presence of the tumour. Nevertheless, a similar procedure could be possibly implemented in those cases in which the tumour boundary is reconstructed from MRI, identifying the cancerous region during the segmentation process. Then, the mesh has been refined along the tumour boundary, where the variables of our problem show the greatest variations. Finally, we employ data from DTI in order to build the diffusion tensor $\mathbb{D}_0$. In order to include these data in our model, the six images coming from DTI and corresponding to the six independent components of the diffusion tensor need to be aligned with the ones from MRI (i.e., they should be shifted, rotated and eventually rescaled in order to perfectly overlay with the MR images). This process can be done using the software *FSL* (*FMRIB Software Library*) [39]. Once all the images are aligned, it is possible to integrate the six components of the tensor $\mathbb{D}_0$ into the computational mesh built upon MRI data, using the scripts implemented in *VMTK* software library [93]. A Z-normal slice of all components of $\mathbb{D}_0$ is reported in Fig. 2 on the left. For further details about the construction of the computational mesh, we refer the reader to [1, 24, 62].

4 Numerical simulations in the brain

We apply the model presented in Section 2.2 to describe the growth of a tumour with an initial radius of 7 mm for a period of 80 days. The simulations have been performed using the discretisation method described in Section 3.2, implemented in the software *FEniCS* [5, 38, 61], which provides a high-level Python and C++ interface for solving PDEs through the Finite Element Method and allows to quickly translate weak formulations into finite element code. In Fig. 3 we show the results in terms of magnitude of the displacement vector $\|\mathbf{u}_s\|$, pressure p and nutrient concentration c_n, while in Fig. 4 we plot the scalar field g, the cell volume fraction ϕ_s and the volumetric solid Cauchy stress $\sigma := -\frac{1}{3}\mathrm{tr}(\mathbb{T}_s)$, along three sagittal, axial, and coronal planes centered within the tumour.

All these results highlight the anisotropic evolution of the tumour inside the healthy tissue. in particular, for what concerns the displacement, it presents an evident anisotropic behaviour and the maximum of its magnitude reaches 6.4 mm. Hence, at the end of the simulation, the final radius is almost doubled compared to the initial one of 7 mm. In Table 3 we report the maximum and the minimum displacement values along all directions of the axes. Furthermore, the final volume is significantly increased, as it reaches the value of about 11.5 cm^3, while the initial one was eight times smaller. Using these data, it is possible to compute an average velocity of radial expansion (VRE), which is based on the variation of the radius during growth. Considering the tumour as a sphere, even if it is not exactly the case due to anisotropy, we obtain a VRE value of about 31.94 mm/year, which is biologically feasible and shows good agreement with experimental measurements reported in

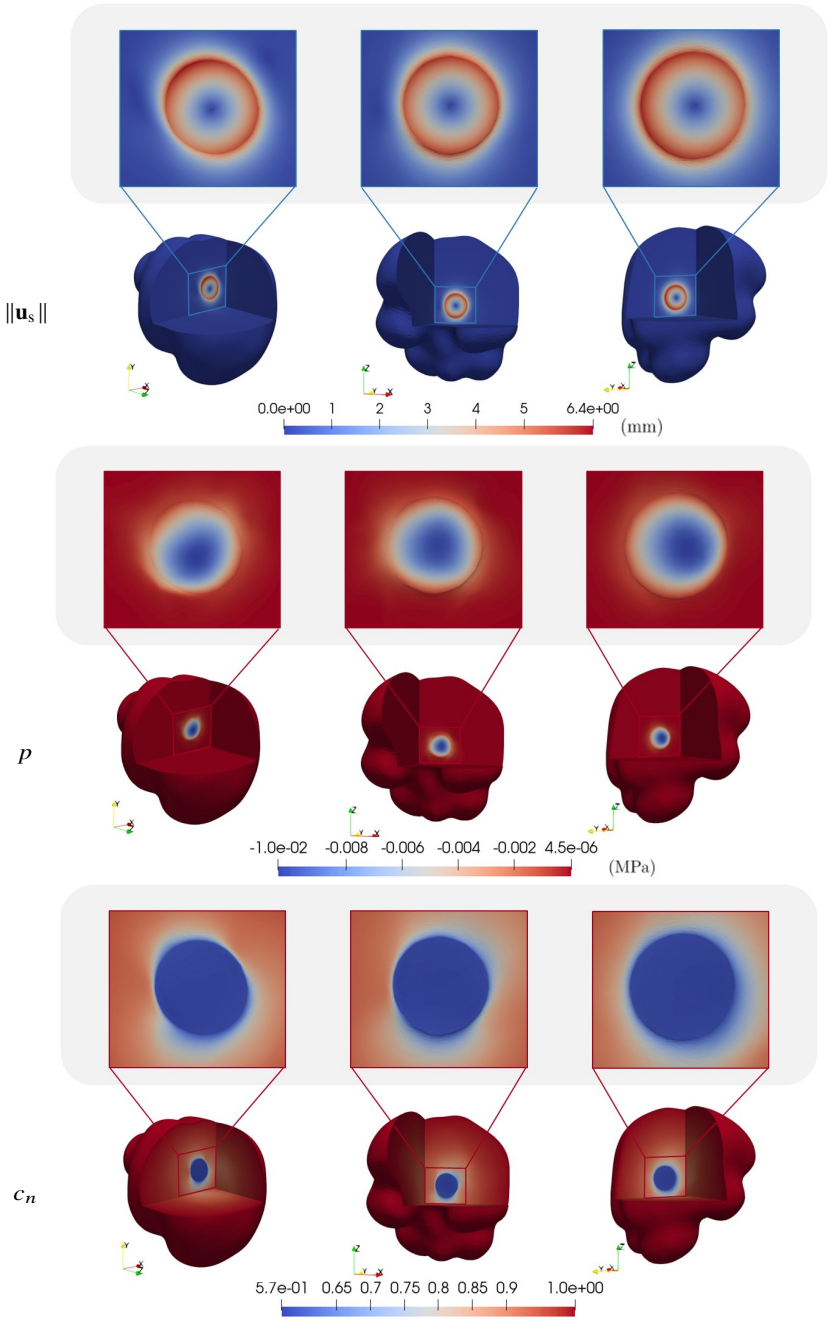


Fig. 3 Comparison between the displacement magnitude $\|\mathbf{u}_s\|$, the pressure p and nutrients c_n after $t = 80$ days of tumour growth in the brain, clipped along three different planes (XY, XZ and YZ respectively).

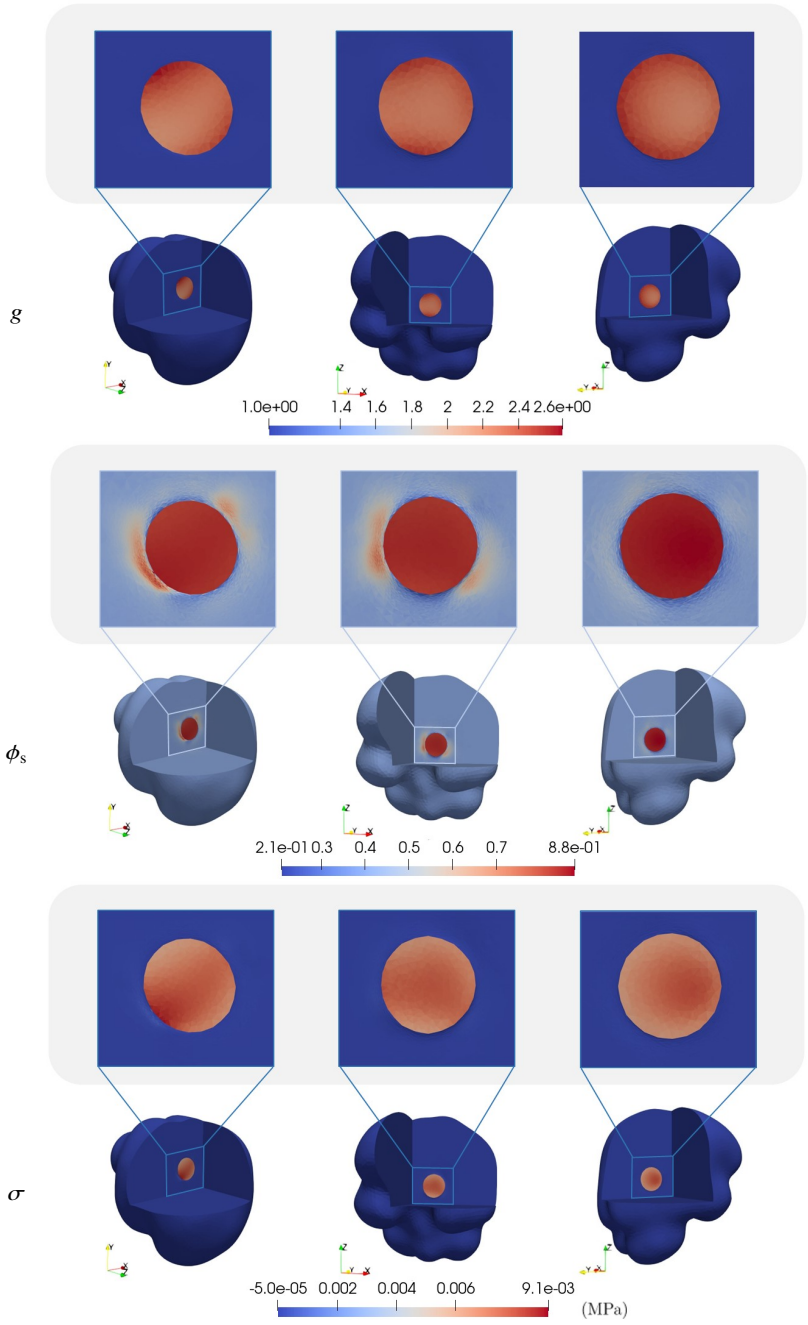


Fig. 4 Comparison between the scalar field g, the cell volume fraction ϕ_s and the stress measure σ after $t = 80$ days of tumour growth in the brain, clipped along three different planes (XY, XZ and YZ respectively).

[81]. Furthermore, the magnitude of displacement along different representative

	X	Y	Z
Min	−5.58 mm	−5.30 mm	−5.85 mm
Max	5.53 mm	6.16 mm	5.93 mm

Table 3 Maximum and minimum displacement values along each direction at time $t = 80$ days.

rays originating from the tumour center is shown in Fig. 5. First of all, it is possible to notice the anisotropic behaviour of the growth, which is enhanced along certain directions. In addition, the displacement has a peak at the tumour boundary and then it undergoes a rapid decrease. However, the graph shows a slight displacement even at 30 mm from the tumour center, meaning that tumour growth affects the surrounding brain tissue up to that distance. Moreover, for what concerns the pressure in Fig. 3,

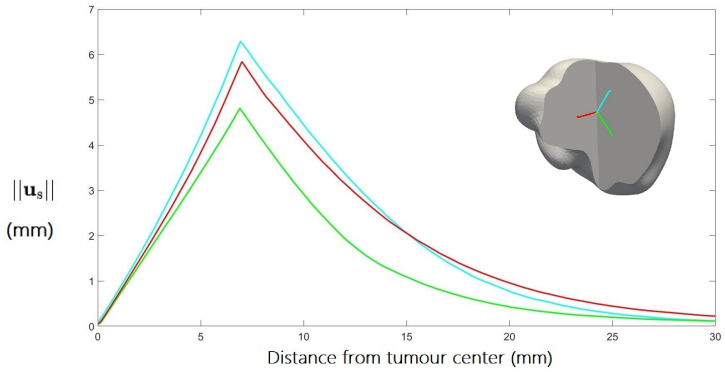


Fig. 5 Comparison of the displacement along three different rays originating from the tumour center.

negative values are shown in the tumour zone since the fluid is consumed during the uncontrolled cellular proliferation. Regarding the concentration of nutrients, it decreases inside the tumour and close to its boundary, while it is maintained at the physiological value of 1 far from the cancer region. We observe that, for the chosen set of parameters, the concentration of nutrients is never above the physiological threshold. The volumetric fraction of the cell phase ϕ_s (Fig. 4) increases in an anisotropic way, but it does not reach the value of ϕ_{max}, for which the contact inhibition of growth occurs. We remark that, since the growth in the tumour region is assumed isotropic, the anisotropic distribution of the cell volume fraction in the healthy tissue is determined by the motion of cells due to tissue solid compression and to fluid pressure. This value is thus influenced by many factors, among which the value of the permeability, the preferential directions of the fibres in the tissue, the growth term and the mechanical properties of the healthy and tumour tissue. For

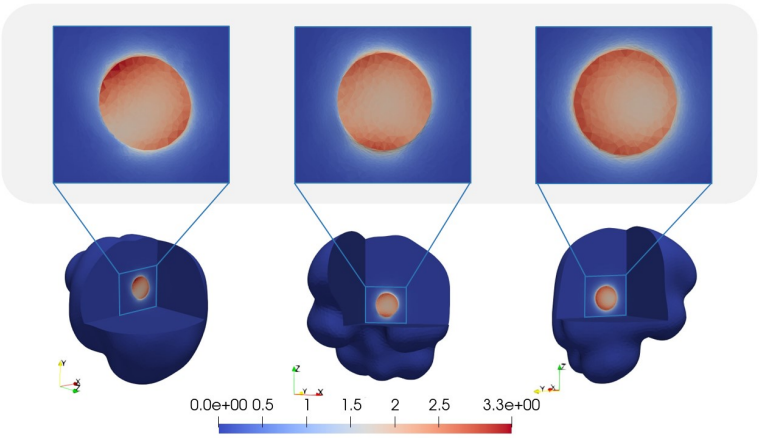


Fig. 6 Frobenius norm about DTI data modification due to tumour growth

the parameters set in the numerical simulations and the patient-specific DTI data, in regions where the tumour boundary displacements are the higher, the healthy cells dislocate circumferentially and fluids tend to accumulate close to the tumour border. Furthermore, the positive value of σ inside the tumour region denotes that the tissue is in compression in this area, while the negative values of σ around the cancer mass underline that the tissue is in traction.

In conclusion, we show some results related to the DTI data modification due to tumour growth. In fact, the expansion of the mass and the induced displacement alter the fibre tracts in the surroundings. Thanks to our model, we can quantify these changes, which significantly affect the diffusion and the preferential directions tensor. In order to compare the differences between $\mathbb{D}_0$ and $\mathbb{D}$ at the last time step ($t = 80$ days), we plot in Fig. 6 the Frobenius norm

$$\frac{\|\mathbb{D} - \mathbb{D}_0\|_F}{\|\mathbb{D}_0\|_F}.$$

It can be noted that the variations in the diffusion data are non-uniform in the tumour area, with the highest variations occurring close to the boundary of the growing cancer, where the tissue experiences the most relevant displacements. Moreover, we also investigate the variation in the eigenvector direction $\mathbf{e}_1^0$ associated with the greatest eigenvalue λ_1^0 of the diffusion tensor $\mathbb{D}_0$. With the aim of reconstructing how much the principal direction is deformed, we express $\mathbf{e}_1^0$ and the eigenvector associated with the greatest eigenvalue of $\mathbb{D}$ using the spherical coordinates (r, φ, θ), where $\varphi \in [0, \pi]$ is the polar angle and $\theta \in [-\pi, \pi]$ is the azimuthal angle. Then we compute the absolute variations of the angles φ and θ between the two eigenvectors, identifying among themselves the polar and azimuthal angles differing by multiples of π. Furthermore, we have properly rescaled the angles variation between 0 and $\frac{\pi}{2}$. As we can notice in Fig. 7, there exist regions in which the two angles defining

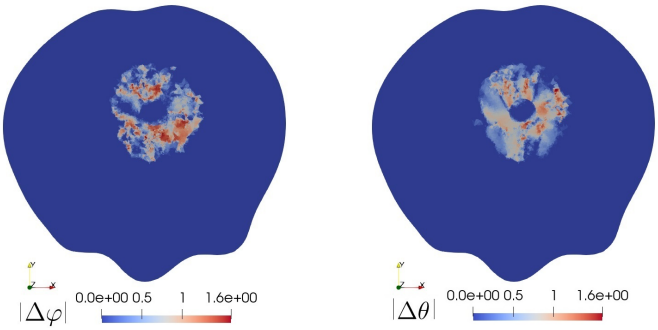


Fig. 7 Variation during tumour growth of the eigenvector associated with the greatest eigenvalue of the diffusion tensor $\mathbb{D}$, quantified in terms of absolute variations of the polar angle $|\Delta\varphi|$ and the azimuthal angle $|\Delta\theta|$.

the spherical coordinates of the two eigenvectors have significant variations. Hence, this leads to relevant changes in the arrangement of fibres and in the preferential direction of nutrients diffusion.

Conclusions and future developments

The investigation of brain tumour growth through mathematical models has attracted a great interest in recent years. However, the quantification of the mechanical impact due to a neoplastic mass inside the brain is still a challenging problem, which has not been addressed extensively. To shed light on this issue, we have proposed a mathematical and computational framework, grounded on Continuum Mechanics and mixture theory, which is able to incorporate medical imaging data. In particular, our model is able to provide a detailed description of brain tumour mass effect, by quantifying the displacements, the solid stress, and the fluid pressure associated with cancer growth in a realistic brain geometry. Such mechanical quantities are usually very difficult to be evaluated *in vivo*. However, their knowledge is fundamental to understand how the growing tumour affects the surrounding tissues, as well as to capture the brain area influenced by the cancer.

An additional feature embedded in our framework is the possibility of incorporating DTI data to account for real diffusion patterns and for the anisotropy of white matter fibres inside the brain. This allows to build diffusion and permeability tensors based on neuroimaging data, which is a relevant step towards a patient-specific personalisation of the model. Moreover, we have shown that our mechanical set-up can be advantageously employed to describe how such tensors are modified due to the tumour mass expansion. Indeed, the growth of the cancer modifies the surrounding orientation of white matter fibres, along which diffusion and fluid motion preferentially happen. A detailed knowledge of all the mechanical variables permits

then to keep track of such changes, which otherwise should be evaluated directly through several imaging scans at different instants of time. Finally, we have provided a numerical algorithm able to represent discontinuous deformation gradients, through the use of a mesh conforming to the sharp host-tumour material interface. Simulations have been performed using the Python-based platform FEniCS, which allows to implement a weak formulation of the equations in a flexible way.

Our results on a prototype brain mesh, reconstructed from real medical data, suggest the feasibility of the model to reproduce anisotropic growth patterns. Moreover, a quantification of tumour-induced displacements and solid stresses clearly highlights the substantial mechanical impact that a proliferating mass may exert onto the surrounding healthy tissue. In particular, our simulations show a displacement magnitude due to tumour growth of about 6.4 mm after 80 days, which may have harmful effects on a patient. Moreover, a displacement of a few millimetres can be found also in regions even 20 mm distant from the tumour boundary. As a consequence, even distal areas of the brain might be affected by the growing mass and withstand unnatural deformations. Finally, we have highlighted how the diffusion tensor and the preferential directions of diffusion are altered by the spread of the cancer.

Although the framework presented in the Chapter is focused on brain tumours, its mathematical foundations remain very general. Therefore, it could also be adapted to other tissues exhibiting anisotropic structures, which may undergo changes subsequent to tumour proliferation.

However, there are still some issues that should be addressed in future research developments. First of all, the prediction of the model should be validated by simulating the growth of a tumour located in the diagnosed region and by comparing the in-silico evolution with the clinical one. This task would require the acquisition of different images during the clinical evolution of the pathology, possibly starting from a tumour in the early stage, so that the DTI data will not be corrupted by the growing mass yet. Indeed, the problem of reconstructing DTI coefficients, and consequently a realistic anisotropy inside and close to the tumour region, is not trivial, since medical imaging data are often isotropic in the diseased region due to fibres disruption. Then, it would be interesting to model therapies, in order to evaluate their effects in the treatment of brain tumours. In addition, simulations of resection may take advantage of the proposed mechanical description, to account for deformations happening when the tumour mass is surgically removed. Finally, another possible improvement might be represented by the inclusion of an anisotropic growth tensor.

Acknowledgements

This work was supported by the MUR, through the project PRIN2017 n. 2017KL4EF3 and through the grant Dipartimenti di Eccellenza 2018–2022 project n. E11G18000350001. GL acknowledges the support of the National Group of Mathematical Physics (GNFM–INdAM) through the INdAM–GNFM project *Progetto Giovani 2023*, n. CUPE53C22001930001. AB acknowledges the support of the INdAM Research

group GNCS through the grant *Progetti di Ricerca 2022*.
Computational resources were provided by HPC@POLITO (http://hpc.polito.it). The neuroimaging data used in this study are gently provided by Dr. Francesco Acerbi and Dr. Alberto Bizzi (Istituto Neurologico Carlo Besta, Milan, Italy).
The authors are indebted to Prof. Pasquale Ciarletta for helpful discussions and support on the work.

References

1. A. Agosti, C. Cattaneo, C. Giverso, D. Ambrosi, and P. Ciarletta: A computational framework for the personalized clinical treatment of glioblastoma multiforme. *ZAMM*, 98:2307–2327 (2018).
2. A. Agosti, C. Giverso, E. Faggiano, A. Stamm, and P. Ciarletta: A personalized mathematical tool for neuro-oncology: A clinical case study. *International Journal of Non-Linear Mechanics*, 107:170–181 (2018).
3. A. Agosti, P. Ciarletta, H. Garcke, and M. Hinze: Learning patient-specific parameters for a diffuse interface glioblastoma model from neuroimaging data. *Mathematical Methods in the Applied Sciences*, 43(15):8945-8979 (2020).
4. J.C.L. Alfonso, K. Talkenberger, M. Seifert, B. Klink, A. Hawkins-Daarud, K.R. Swanson, H. Hatzikirou, and A. Deutsch: The biology and mathematical modelling of glioma invasion: A review. *Journal of the Royal Society Interface*, 14:1–20 (2017).
5. M.S. Alnaes, J. Blechta, J. Hake, A. Johansson, B. Kehlet, A. Logg, C. Richardson, J. Ring, M.E. Rognes, and G.N. Wells: The FEniCS Project Version 1.5. *Archive of Numerical Software*, 3:9-23 (2015).
6. D. Ambrosi and L. Preziosi: On the Closure of Mass Balance Models for Tumor Growth. *Mathematical Models and Methods in Applied Sciences*, 12(5):737–754 (2002).
7. D. Ambrosi and F. Mollica: On the mechanics of a growing tumor. *International Journal of Engineering Science*, 40:1297–1316 (2002).
8. D. Ambrosi and F. Mollica: The role of stress in the growth of a multicell spheroid. *Journal of Mathematical Biology*, 48:477–499 (2004).
9. S. Angeli and T. Stylianopoulos: Biphasic modeling of brain tumor biomechanics and response to radiation treatment. *Journal of Biomechanics*, 49:1524–1531 (2016).
10. S. Angeli, K.E. Emblem, P. Due-Tonnessen, and T. Stylianopoulos: Towards patient-specific modeling of brain tumor growth and formation of secondary nodes guided by DTI-MRI. *NeuroImage: Clinical*, 20:664–673 (2018).
11. M. Aubert, M. Badoual, S. Fereol, C. Christov and B. Grammaticos: A cellular automaton model for the migration of glioma cells. *Phys. Biol.* 13;3(2):93-100 (2006).
12. M. Aubert, M. Badoual, C. Christov and B. Grammaticos: A model for glioma cell migration on collagen and astrocytes. *J. R. Soc. Interface* 5:75–83 (2008).
13. V. Balbi, A. Trotta, M. Destrade, and A. Annaidh: Poynting effect of brain matter in torsion. *Soft Matter*, 15:5147-5153 (2019).
14. S. Banerjee, S. Khajanchi and S. Chaudhuri: A mathematical model to elucidate brain tumor abrogation by immunotherapy with T11 Target Structure. *PLoS ONE* 10(5): e0123611 (2015).
15. P.J. Basser: Interstitial pressure, volume, and flow during infusion into brain tissue. *Microvascular Research*, 44:143-165 (1992).
16. P.-Y. Bondiau, O. Clatz, M. Sermesant, P.-Y. Marcy, H. Delingette, M. Frenay, and N. Ayache: Biocomputing: numerical simulation of glioblastoma growth using diffusion tensor imaging. *Phys. Med. Biol.*, 53:879-893 (2008).
17. K. Bottger, H. Hatzikirou, A. Chauviere, and A. Deutsch: Investigation of the migration/proliferation dichotomy and its impact on avascular glioma invasion. *Math. Model. Nat. Phenom.*, 7:105-135 (2012).

18. M. Bruehlmeier, U. Roelcke, P. Blauenstein, J. Missimer, P.A. Schubiger, J.T. Locher, R. Pellikka, and S.M. Ametamey: Measurement of the extracellular space in brain tumors using 76br-bromide and PET. *Journal of Nuclear Medicine*, 44:1210–1218 (2003).
19. H. Byrne and L. Preziosi: Modelling solid tumour growth using the theory of mixtures. *Mathematical Medicine and Biology*, 20:341–366 (2003).
20. C. Chatelain, T. Balois, P. Ciarletta, and M. Ben Amar: Emergence of microstructural patterns in skin cancer: a phase separation analysis in a binary mixture. *New Journal of Physics*, 13:115013 (2011).
21. V. P. Chauhan, Y. Boucher, C. R. Ferrone, S. Roberge, J. D. Martin, T. Stylianopoulos, N. Bardeesy, R. A. DePinho, T. P. Padera, L. L. Munn, and R. K. Jain: Compression of pancreatic tumor blood vessels by hyaluronan is caused by solid stress and not interstitial fluid pressure. *Cancer Cell*, 1(26):14-15 (2014).
22. G. Cheng, J. Tse, R. K. Jain, and L. L. Munn: Micro-environmental mechanical stress controls tumor spheroid size and morphology by suppressing proliferation and inducing apoptosis in cancer cells. *PLoS One*, 4(2):1-11 (2009).
23. O. Clatz, M. Sermesant, P. Bondiau, H. Delingette, S.K. Warfield, G. Malandain, and N. Ayache: Realistic simulation of the 3-D growth of brain tumors in MR images coupling diffusion with biomechanical deformation. *IEEE Trans. Med. Imaging*, 24:1334–1346 (2005).
24. M.C. Colombo, C. Giverso, E. Faggiano, C. Boffano, F. Acerbi, and P. Ciarletta: Towards the personalized treatment of Glioblastoma: Integrating patient-specific clinical data in a continuous mechanical model. *PLoS ONE*, 10:e0132887 (2015).
25. M. Conte, L. Gerardo-Giorda, and M. Groppi: Glioma invasion and its interplay with nervous tissue and therapy: A multiscale model. *J. Theor. Biol.*, 486:110088 (2020).
26. M. Conte and C. Surulescu: Mathematical modeling of glioma invasion: acid- and vasculature mediated go-or-grow dichotomy and the influence of tissue anisotropy. *Appl. Math. Comp.*, 407:126305 (2021).
27. M. Destrade, M.D. Gilchrist, J.G. Murphy, B. Rashid, and G. Saccomandi: Extreme softness of brain matter in simple shear. *International Journal of Non-Linear Mechanics*, 75:54-58 (2015).
28. S. Di Stefano, M. Carfagna, M.M M. Knodel, K. Hashlamoun, S. Federico, and A. Grillo: Anelastic reorganisation of fibre-reinforced biological tissues. *Computing and Visualization in Science* 20:95–109 (2019).
29. W. Ehlers and G. Eipper: Finite Elastic Deformations in Liquid-Saturated and Empty Porous Solids. *Transport in Porous Media*, 34:179–191 (1999).
30. W. Ehlers and A. Wagner: Multi-component modelling of human brain tissue: A contribution to the constitutive and computational description of deformation, flow and diffusion processes with application to the invasive drug-delivery problem. *Comput. Methods Biomech. Biomed. Eng.*, 18:861–879 (2015).
31. W. Ehlers, M. M. Rehm, P. Schroder, D. Stohr, and A. Wagner: Multiphasic modelling and computation of metastatic lung-cancer cell proliferation and atrophy in brain tissue based on experimental data. *Biomech. Model. Mechanobiol.*, 21:277-315 (2022).
32. A. Elazab, A. M. Anter, H. Bai, Q. Hu, Z. Hussain, D. Ni, T. Wang and B. Lei: An optimized generic cerebral tumor growth modeling framework by coupling biomechanical and diffusive models with treatment effects. *Applied Soft Computing*, 80:617–627 (2019).
33. C. Engwer, T. Hillen, M. Knappitsch, and C. Surulescu: Glioma follow white matter tracts: A multiscale DTI-based model. *J. Math. Biol.* 71:551-582 (2015).
34. C. Engwer, A. Hunt, and C. Surulescu: Effective equations for anisotropic glioma spread with proliferation: A multiscale approach and comparisons with previous settings. *Math. Med. Biol.*, 33:435-459 (2016).
35. C. Engwer, M. Knappitsch, and C. Surulescu: A multiscale model for glioma spread including cell-tissue interactions and proliferation. *Math. Biosci. Eng.*, 13:443-460 (2016).
36. C. Engwer and M. Wenske: Estimating the extent of glioblastoma invasion. *J. Math. Biol.*, 82:10 (2021).

37. J. Falco, A. Agosti, I.G. Vetrano, A. Bizzi, F. Restelli, M. Broggi, M. Schiariti, F. DiMeco, P. Ferroli, P. Ciarletta, and F. Acerbi: In silico mathematical modelling for glioblastoma: A critical review and a patient-specific case. *J. Clin. Med.*, 10:2169 (2021).
38. The FEniCS Project, https://fenicsproject.org/ (2021).
39. FMRIB Software Library. https://fsl.fmrib.ox.ac.uk/fsl/fslwiki
40. H.B. Frieboes, J.S. Lowengrub, S. Wise, X. Zheng, P. Macklin, E.L. Bearer, and V. Cristini: Computer simulations of glioma growth and morphology. *NeuroImage*, 37:S59–S70 (2007).
41. P. Gerlee and A.R.A. Anderson: An evolutionary hybrid cellular automaton model of solid tumour growth. *Journal of Theoretical Biology*, 246:583–603 (2007).
42. P. Gerlee and S. Nelander: The impact of phenotypic switching on glioblastoma growth and invasion. *PLoS Comp. Biol.*, 8:e1002556 (2012).
43. P. Gerlee and S. Nelander: Travelling wave analysis of a mathematical model of glioblastoma growth. *Math. Biosci.*, 276:75–81 (2016).
44. C. Giverso, M. Scianna, and A. Grillo: Growing avascular tumours as elasto-plastic bodies by the theory of evolving natural configurations. *Mechanics Research Communications*, 68:31–39 (2015).
45. M.E. Gurtin, E. Fried, and L. Anand: The Mechanics and Thermodynamics of Continua. *Cambridge University Press*, (2010).
46. H. Si. Hang: TetGen, a Delaunay-Based Quality Tetrahedral Mesh Generator. *Association for Computing Machinery*, 41(2) 0098-3500 (2015).
47. L. Hathout, V. Patel, and P. Wen: A 3-Dimensional DTI MRI-based model of GBM growth and response to radiation therapy. *Int. J. Oncol.*, 49:1081–1087 (2016).
48. H. Hatzikirou, A. Deutsch, C. Schaller, M. Simon, and K. Swanson: Mathematical Modelling of Glioblastoma Tumour Development: a review. *Mathematical Models and Methods in Applied Sciences*, 15(11):1779–1794 (2005).
49. H. Hatzikirou, D. Basanta, M. Simon, K. Schaller, and A. Deutsch: 'Go or grow': the key to the emergence of invasion in tumour progression?. *Math. Med. Biol.*, 29:49-65 (2012).
50. C. Hogea, C. Davatzikos, and G. Biros: An image-driven parameter estimation problem for a reaction–diffusion glioma growth model with mass effects. *J. Math. Biol.*, 56:793-825 (2008).
51. M.H. Holmes and V.C. Mow: The nonlinear characteristics of soft gels and hydrated connective tissues in ultrafiltration. *J. Biomech.* 23(11):1145-56 (1990).
52. A. Hunt and C. Surulescu: A multiscale modeling approach to glioma invasion with therapy. *Vietnam J. Math.*, 45:221-240 (2016).
53. K.C. Iarosz, F.S. Borges, A.M. Batista, M.S. Baptista, R.A.N. Siqueira, R.L. Viana, S.R. Lopes: Mathematical model of brain tumour with glia–neuron interactions and chemotherapy treatment.' *J. Theor. Biol.*, 368:113-121 (2015).
54. S. Jbabdi, E. Mandonnet, H. Duffau, L. Capelle, K.R. Swanson, M. Pélégrini-Issac, R. Guillevin, and H. Benali: Simulation of anisotropic growth of low-grade gliomas using diffusion tensor imaging. *Magnetic Resonance in Medicine*, 54:616–624 (2005).
55. A. R. Kansal, S. Torquato, G. R. Harsh IV, E. A. Chiocca and T. S. Deisboeck: Simulated brain tumor growth dynamics using a three-dimensional cellular automaton. *J. Theor. Biol.* 203:367–382 (2000).
56. E. Khain, M. Katakowski, S. Hopkins, A. Szalad, X. Zheng, F. Jiang, and M. Chopp: Collective behavior of brain tumor cells: The role of hypoxia. *Phys. Rev. E*, 83:031920 (2011).
57. Y. Kim, G. Powathil, H. Kang, D. Trucu, H. Kim, S. Lawler, and M. Chaplain: Strategies of eradicating glioma cells: A multi-scale mathematical model with miR451-AMPK-mTOR Control. *PLoS ONE*, 10:e0114370 (2015).
58. Y. Kim, H. Kang, G. Powathil, H. Kim, D. Trucu, W. Lee, S. Lawler, and M. Chaplain: Role of extracellular matrix and microenvironment in regulation of tumor growth and LAR-mediated invasion in glioblastoma. *PLoS ONE*, 13:e0204865 (2018).
59. S.K. Kyriacou, C. Davatzikos, S.J. Zinreich, and R.N. Bryan: Nonlinear elastic registration of brain images with tumor pathology using a biomechanical model. *IEEE Trans. Med. Imaging*, 18(7):580-592 (1999).

60. J. Lipkova, B. Menze, B. Wiestler, P. Koumoutsakos, and J.S. Lowengrub: Modelling glioma progression, mass effect and intracranial pressure in patient anatomy. *J. R. Soc. Interface*, 19:20210922 (2022).
61. A. Logg, K.-A. Mardal, G. N. Wells et al.: Automated solution of differential equations by the Finite Element Method. Springer (2012).
62. G. Lucci, A. Agosti, P. Ciarletta, and C. Giverso: Coupling solid and fluid stresses with brain tumour growth and white matter tract deformations in a neuroimaging-informed model. *Biomech. Model. Mechanobiol.*, 21:1483–1509 (2022).
63. Y. Mansury, M. Kimura, J. Lobo, and T.S. Deisboeck: Emerging patterns in tumor systems: Simulating the dynamics of multicellular clusters with an agent-based spatial agglomeration model. *J. Theor. Biol.*, 219:343-370 (2002).
64. Y. Mansury and T.S. Deisboeck: The impact of "search precision" in an agent-based tumor model. *J. Theor. Biol.*, 224:325-337 (2003).
65. Y. Mansury and T. S. Deisboeck: Modelling tumours as complex biosystems: An agent-based approach, in Complex Systems Science: The Emergence of a New Approach in BioMedicine. *Kluwer* (2004).
66. N.L. Martirosyan, E.M. Rutter, W.L. Ramey, E.J. Kostelich, Y. Kuang, and M.C. Preul: Mathematically modeling the biological properties of gliomas: a review. *Math. Biosci. Eng.*, 12:879–905 (2015).
67. P. Mascheroni, S. Stigliano, M. Carfagna, D.P. Boso, L. Preziosi, P. Decuzzi, and B.A. Schrefler: Predicting the growth of glioblastoma multiforme spheroids using a multiphase porous media model. *Biomech. Model. Mechanobiol.*, 15:1215–1228 (2016).
68. P. Mascheroni, M. Carfagna, A. Grillo, D.P. Boso, and B.A. Schrefler: An avascular tumor growth model based on porous media mechanics and evolving natural states. *Mathematics and Mechanics of Solids*, 23:686–712 (2018).
69. L.A. Mihai, S. Budday, G.A. Holzapfel, E. Kuhl and A. Goriely: A family of hyperelastic models for human brain tissue. *Journal of the Mechanics and Physics of Solids*, 106:60–79 (2017).
70. H.T. Nia, H. Liu, G. Seano, M. Datta, D. Jones, N. Rahbari, J. Incio, V.P. Chauhan, K. Jung, J.D. Martin, V. Askoxylakis, T.P. Padera, D. Fukumura, Y. Boucher, F.J. Hornicek, A.J. Grodzinsky, J.W. Baish, L.L. Munn, and R.K. Jain: Solid stress and elastic energy as measures of tumour mechanopathology. *Nat. Biomed. Eng.*, 1:0004 (2017).
71. H. T. Nia, M. Datta, G. Seano, S. Zhang, W. W. Ho, S. Roberge, P. Huang, L. L. Munn, and R. K. Jain: In vivo compression and imaging in mouse brain to measure the effects of solid stress. *Nat. Protoc.*, 15(8):2321-2340 (2020).
72. R.W. Ogden: Large deformation isotropic elasticity - on the correlation of theory and experiment for incompressible rubberlike solids. *Proceedings of the Royal Society of London*, 326:565–584 (1972).
73. K.J. Painter and T. Hillen: Mathematical modelling of glioma growth: The use of diffusion tensor imaging (DTI) data to predict the anisotropic pathways of cancer invasion. *J. Theor. Biol.*, 323:25–39 (2013).
74. T.P. Prevost, A. Balakrishnan, S. Suresh, and S. Socrate: Biomechanics of brain tissue. *Acta Biomaterialia*, 7:83-95 (2011).
75. K. R. Rajagopal and L. Tao: Mechanics of mixtures. *World Scientific Publishing Co Pte Ltd*, (1995).
76. R. Rockne, E.C. Alvord Jr., J.K. Rockhill, and K.R. Swanson: A mathematical model for brain tumor response to radiation therapy. *J. Math. Biol.*, 58:561–578 (2009).
77. L. M. Sander and T. S. Deisboeck: Growth patterns of microscopic brain tumours. *Phys. Rev. E*, 66:051901 (2002).
78. G. Seano, H. T. Nia, K. E. Emblem, M. Datta, J. Ren, S. Krishnan, J. Kloepper, M. C.Pinho, W. W. Ho, M. Ghosh, V. Askoxylakis, G. B. Ferraro, L. Riedemann, E. R. Gerstner, T. T. Batchelor, P. Y. Wen, N. U. Lin, A. J. Grodzinsky, D. Fukumura, P. Huang, J. W. Baish, T. P. Padera, L. L. Munn, and R. K. Jain: Solid stress in brain tumours causes neuronal loss and neurological dysfunction and can be reversed by lithium. *Nat. Biomed. Eng.*, 3(3):230-245 (2019).

79. Slicer3D, image computing platform. https://www.slicer.org/
80. T.C. Steed, J.M. Treiber, M.G. Brandel, K.S. Patel, A.M. Dale, B.S. Carter, and C.C. Chen: Quantification of glioblastoma mass effect by lateral ventricle displacement. *Sci. Rep.*, 8:2827 (2018).
81. A.L. Stensjøen, O. Solheim, K.A. Kvistad, A.K. Haberg, Ø. Salvesen, and E.M. Berntsen: Growth dynamics of untreated glioblastomas in vivo. *Neuro-Oncology*, 17(10):1402-1411 (2015).
82. S. Suveges, K. Hossain-Ibrahim, J.D. Steele, R. Eftimie, and D. Trucu: Mathematical modelling of glioblastomas invasion within the brain: A 3D multi-scale moving-boundary approach. *Mathematics*, 9:2214 (2021).
83. A. Swan, T. Hillen, J.C. Bowman, and A.D. Murtha: A patient-specific anisotropic diffusion model for brain tumour spread. *Bull. Math. Biol.*, 80:1259-1291 (2018).
84. K.R. Swanson, E.C. Alvord Jr., and J.D. Murray: A quantitative model for differential motility of gliomas in grey and white matter. *Cell Proliferation*, 33:317–329 (2000).
85. K.R. Swanson, E.C. Alvord Jr., and J.D. Murray: Virtual brain tumours (gliomas) enhance the reality of medical imaging and highlight inadequacies of current therapy. *British Journal of Cancer*, 86:14–18 (2002).
86. K.R. Swanson, E.C. Alvord Jr., and J.D. Murray: Quantifying efficiency of chemotherapy of brain tumors with homogeneous and heterogeneous drug delivery. *Acta Biotheor.*, 50:223–237 (2002).
87. K.R. Swanson, C. Bridge, J.D. Murray, and E.C. Alvord Jr.: Virtual and real brain tumors: using mathematical modeling to quantify glioma growth and invasion. *Journal of the Neurological Sciences*, 216:1–10 (2003).
88. K.R. Swanson, E.C. Alvord Jr., and J.D. Murray: Virtual resection of gliomas: effect of extent of resection on recurrence. *Math. Comput. Model.*, 37:1177–1190 (2003).
89. K.R. Swanson, R.C. Rockne, J. Claridge, M.A. Chaplain, E.C. Alvord Jr., and A.R. Anderson: Quantifying the role of angiogenesis in malignant progression of gliomas: In silico modeling integrates imaging and histology. *Cancer Res.*, 71:7366–7375 (2011).
90. M.L. Tanaka, W. Debinski, and I.K. Puri: Hybrid mathematical model of glioma progression. *Cell Proliferation*, 42:637–646 (2009).
91. M. Tektonidis, H. Hatzikirou, A. Chauvière, M. Simon, K. Schaller, and A. Deutsch: Identification of intrinsic in vitro cellular mechanisms for glioma invasion. *J. Theor. Biol.*, 287:131-147 (2011).
92. P. Tracqui, C.G. Cruywagen, D.E. Woodward, G.T. Bartoo, J.D. Murray, and E.C. Alvord Jr.: A mathematical model of glioma growth: the effect of chemotherapy on spatiotemporal growth. *Cell Prolif.*, 28:17-31 (1995).
93. VMTK, The Vascular Modeling Toolkit. http://www.vmtk.org/
94. D.E. Woodward, J. Cook, P. Tracqui, C.G. Cruywagen, J.D. Murray, and E.C. Alvord Jr.: A mathematical model of glioma growth: the effect of extent of surgical resection. *Cell Prolif.*, 29:269–288 (1996).
95. K. Yangjin, J. Hyejin, and H. Othmer: The role of the tumor microenvironment in glioblastoma: A mathematical model. *IEEE Trans. Biomed. Eng.*, 64:519–527 (2017).
96. L. Zhang, C.G. Strouthos, Z. Wang, and T.S. Deisboeck: Simulating brain tumor heterogeneity with a multiscale agent-based model: Linking molecular signatures, phenotypes and expansion rate. *Math. Comp. Model.*, 49:307–319 (2009).